Tracking L1 C/A and L2C Signals through Ionospheric Scintillations

by Mark L. Psiaki, Todd E. Humphreys, Alessandro P. Cerruti, Steven P. Powell, and Paul M. Kintner, Jr.
Cornell University, Ithaca, N.Y., 14853-7501, U.S.A.

BIOGRAPHIES

Mark L. Psiaki is a Professor in the Sibley School of Mechanical and Aerospace Engineering. He received a B.A. in Physics and M.A. and Ph.D. degrees in Mechanical and Aerospace Engineering from Princeton University. His research interests are in the areas of estimation and filtering, spacecraft attitude and orbit determination, and GNSS technology and applications.

Todd E. Humphreys is postdoctoral associate in the Sibley School of Mechanical and Aerospace Engineering. He received his B.S. and M.S. degrees in Electrical and Computer Engineering from Utah State University and his Ph.D. degree in Aerospace Engineering from Cornell University. His research interests are in estimation and filtering, spacecraft attitude determination, GNSS technology, and GNSS-based study of the ionosphere and neutral atmosphere.

Alessandro P. Cerruti is currently a Ph.D. candidate with the Space Physics and Engineering Group in the School of Electrical and Computer Engineering. His primary interest is space weather and its effects on GNSS receiver operation.

Steven P. Powell is a Senior Engineer with the Space Plasma Physics Group in the Department of Electrical and Computer Engineering. He has M.S. and B.S. degrees in Electrical Engineering from Cornell University. He has been involved with the design, fabrication, and testing of several GNSS receivers.

Paul M. Kintner, Jr. is a Professor of Electrical and Computer Engineering. He received a B.S in Physics from the University of Rochester and a Ph.D. in Physics from the University of Minnesota. His research interests include the electrical properties of upper atmospheres, space weather, and developing GNSS instruments for space science. He is a Fellow of the APS.

ABSTRACT

Phase-lock loops are being developed and tested for robust tracking of the GPS L1 C/A and L2C CL signals through strong ionospheric scintillations. This work is part of an effort to design robust dual-frequency scintillation monitors that exploit the characteristics of the new civilian signals which are appearing on the GPS L2 frequency. Three new features increase L2 carrier tracking robustness in comparison to current civilian dual-frequency GPS receivers. The first feature is open access to the transmitted L2C PRN codes, which enables the tracking algorithm to eliminate the squaring loss of current semicodeless dual-frequency civilian receivers. The second feature is the use of the L2C CL pilot signal, which avoids a second source of squaring loss inherent in the removal of unknown navigation data bits. The third feature is a new PLL architecture that is based on a Kalman filter and that generalizes the notion of a discriminator in a way that tends to reduce cycle slipping. The new tracking loops have been tested on equatorial scintillation data that have been collected using a dual-frequency wide-band digital storage receiver. The new L2 tracking loop performs well, but the data did not provide a significant tracking challenge because the highest S_4 index was 0.51. Additional tests have been performed on the L1 and L2 tracking loops using a simulation that includes a high-fidelity physics-based scintillation model. These tests demonstrate that the new phase-lock loops can track robustly, with only intermittent cycle slips, through scintillations with intensities up to $S_4 = 1$.

INTRODUCTION

Ionospheric scintillation in the equatorial region is a phenomenon in which short-length-scale electron density variations give rise to signal diffraction that results in rapid changes in the power and carrier phase of received GNSS signals. The most severe scintillations tend to occur near the magnetic equator or at high latitudes [1]. The rapidity and magnitude of the signal fluctuations often cause GNSS receivers to lose lock on the scintillating signal [2,3,4,5]. This loss of lock causes a total loss of data from the received signal.

There is a significant interest in the development of GNSS receivers that can track through scintillations more reliably than can current receivers. Such improvements would make Position, Navigating and Timing (PNT) operations more dependable in a scintillating environment. The terms "robust" and "robustness" will be used throughout this paper in order to characterize

Preprint from ION GNSS 2007

tracking algorithms that operate reliably during strong scintillations. This paper's goal is to develop and test new tracking algorithms that offer significant increases in robustness.

The authors' interest in scintillations and in robust tracking through scintillations stems from their ongoing efforts to use GNSS technology in order to remotely sense the ionospheric disturbances that cause this phenomenon [6,7,8,9]. An improved ability to track GNSS signals through ionospheric scintillations would constitute an important aid to their efforts to use GNSS technology as a tool for studying the disturbed ionosphere. Their studies specifically seek to probe the strongest possible scintillations. Therefore, they require the highest degree of robustness in order to be able to monitor and characterize the most severe possible scintillations.

A new scintillation science experiment that is under development provides the motivation for the current effort to design dual-frequency GPS receivers that track signals very robustly. This project's goal is to image the ionospheric density variations that cause equatorial scintillations. It seeks to do this by using scintillating dual-frequency GPS signals as the inputs to a diffraction tomography calculation. The concept of this experiment is illustrated in Fig. 1. An array of GNSS receivers will be distributed along a (magnetic-) east/west line below the equatorial ionosphere. This array will record the time-varying signal power and carrier phase variations that are caused by scintillations at the L1 and L2 frequencies. These dual-frequency amplitude and phase data will be the inputs to a model-inversion/estimation algorithm. That algorithm will use a wave propagation physical model of how ionospheric electron density variations give rise to signal scintillations at the receiver. It will estimate the density variations by iteratively computing the density profile that best reproduces the recorded scintillation data when propagated through its physical model.

The feasibility of conducting such an experiment for strong ionospheric scintillations is critically dependent on the availability of inexpensive civilian dual-frequency GNSS receivers that can track though strong scintillations robustly. Unfortunately, current civilian dual-frequency receivers must rely on semicodeless processing of the encrypted military P(Y) code in order to track the L2 signal. This technology is inherently prone to loss of lock, and receivers that use it regularly experience tracking problems during scintillations [4,5].

The present study is part of an ongoing effort by the authors to develop receivers with significantly improved tracking robustness during scintillations [3,10,11]. Its main goal is to develop a new carrier tracking phase-lock loop (PLL) that exploits the properties of the new L2C signals in order to achieve greatly enhanced L2 tracking robustness. The two significant properties that can enhance tracking robustness are the presence of non-encrypted CM and CL PRN codes and the lack of data bits on the CL pilot code.

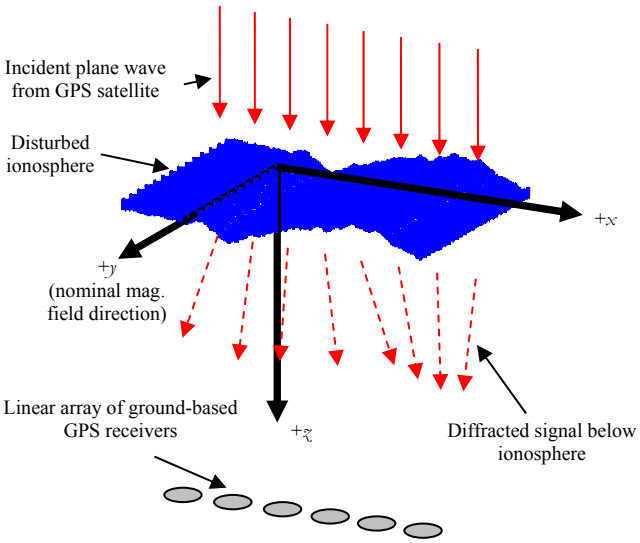

Fig. 1. Schematic diagram of proposed diffraction tomography experiment to image the disturbed scintillating ionosphere based on data from an east-west array of ground-based GPS receivers.

Current state-of-the-art dual-frequency civilian receivers track the L2 signal by performing a cross-correlation with the P(Y) code on the L1 signal, which incurs a squaring loss. A tracking loop with a squaring loss tends to degrade in accuracy and lose lock much more rapidly as power decreases than does a non-squaring loop. In scintillations, where power can fade on L1 and L2, the tracking difficulties for a semicodeless loop that operates on the L2 P(Y) signal are very pronounced because the squaring loss is a function of the power on both GPS frequencies. Receivers that use the new L2C civilian signals experience no such difficulties because the signals' known PRN codes eliminate the need for cross-correlation.

A second form of squaring loss occurs when unknown navigation data bits must be wiped off of the signal before it can be used in a tracking loop. Loops that track the L1 C/A signal experience this loss when they wipe off the 50 Hz navigation data bits. The L2C signal includes two PRN codes, the CM code and the CL code. They are time-multiplexed on an every-other-chip basis [12]. The CM signal carries unknown data bits, but the CL signal is a dataless pilot signal. It can be used independently of the CM signal in order to implement a non-squaring PLL that tracks the L2 signal's carrier phase.

The contributions of the present study are to develop a new non-squaring PLL for the L2C CL signal and to test it under scintillation conditions. Two types of test have

been carried out. One applies the PLL to dual-frequency wide-band data that have been collected during actual equatorial scintillations. The other applies the PLL in a physics-based simulation of dual-frequency scintillations. This simulation uses a scintillation model that is based on a phase screen calculation [13,14]. The goal of the tests is to determine whether the new PLL will improve a receiver's ability to track the L2 signal during scintillations. The tests also study the scintillation robustness of an L1 C/A signal PLL and of a semicodeless L2 P(Y) PLL. This latter PLL is implemented using a method of semicodeless accumulation calculation that is called "Soft-Decision Z-tracking" [15].

The authors' primary scintillation experience has been gained in the equatorial region. Equatorial scintillations are characterized by rapid fluctuations in both the power and the carrier phase of the received GNSS signal. These differ from high-latitude scintillations, in which the primary disturbances are in the carrier phase. This paper deals exclusively with equatorial scintillations. Although it is quite possible that the paper's methods and results would carry over to high-latitude scintillations, the paper itself makes no attempt to demonstrate any applicability to the high-latitude case.

The remainder of this paper is divided into 5 sections plus conclusions. Section II reviews the characteristics of scintillations and the difficulty of carrier tracking through strong scintillations. Section III presents a new non-squaring PLL for tracking the L2C CL signal. This section also describes two variants of the L2C PLL that are considered for comparison purposes: a version that involves data bit wipe-off for tracking the L1 C/A signal and a version for semicodeless tracking of the L2 P(Y) signal. Section IV describes a scintillation data collection campaign and how the data have been used to evaluate the performance of the L2C CL PLL and the L1 C/A PLL during moderate scintillations. Section V describes a phase screen simulation that has been developed in order to study tracking under severe scintillation conditions. Section VI presents the results of the tracking studies, both for the real scintillation data and for the simulated data. Section VII gives a summary of the paper's contributions and presents its conclusions. The appendix contains additional details about the implementation of the phase screen simulation.

II. THE DIFFICULTY OF CARRIER TRACKING DURING EQUATORIAL SCINTILLATIONS

A. Canonical Fades

The most significant feature of equatorial scintillations from the standpoint of carrier tracking is a phenomenon that has been given the label "Canonical Fade" [11]. Three canonical fades are highlighted in Fig. 2. This figure plots the normalized power time history and the de-trended carrier phase time history that occurred during severe equatorial scintillations of a GPS L1 signal [10].

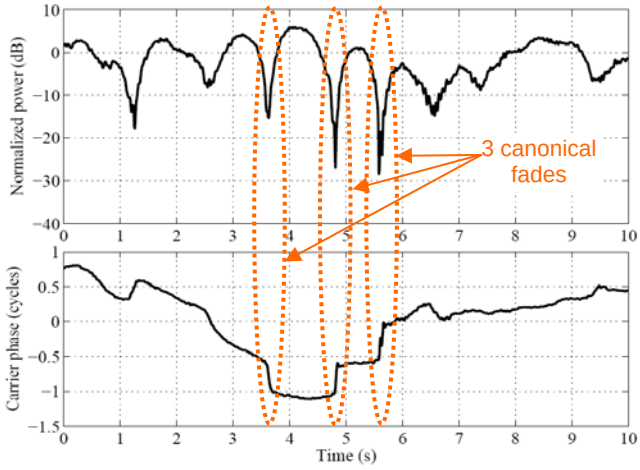

Fig. 2. *Canonical fades as seen in a GPS L1 C/A signal's power time history (top plot) and de-trended carrier phase time history (bottom plot) ($S_4 \approx 0.9$).*

Each canonical fade consists of a rapid, deep power fade (see top plot) accompanied by an abrupt phase change of +/- ½ carrier cycle (see bottom plot). It is certain that these carrier cycle changes are real. They are not the results of half-cycle tracking loop slips due to erroneous decoding of the 50 Hz navigation data bits because the off-line MATLAB software receiver that processed these data had knowledge of the bits and had wiped them off before tracking the signal. Further confirmation of the canonical fade phenomenon has been obtained by considering scintillation data from the Wideband satellite mission [11].

Canonical fades present an extreme challenge to a carrier tracking loop such as a PLL. A PLL relies on feedback of a measurement of its carrier phase error in order to track a signal. This measurement is based in-phase (I) and quadrature (Q) accumulations that are used to compute a discriminator value that is an indication of carrier phase error. The phase measurement error varies inversely with the square root of the received signal power. Therefore, the phase measurement error is the largest during the deep canonical power fades. Unfortunately, this is exactly the time when the PLL needs to have the best possible carrier phase measurements in order to accurately discern which way the rapid half-cycle carrier phase jump is about to go. In other words, the PLL has the poorest information about carrier phase at precisely the moment when it needs the best possible information in order to track the rapid changes of phase. This combination tends to lead to cycle slipping and, if the scintillations are severe enough, eventually to complete loss of the signal due to loss of frequency lock.

B. The Advantage of using a Pilot Signal to track through Equatorial Scintillations

One advantage of the L2C CL signal for scintillation tracking is its lack of navigation data bits. This advantage is illustrated in Fig. 3, which plots measured points in the [*I*;*Q*] plane for actual scintillating L1 C/A and L2C CL signals. Each [*I*;*Q*] pair provides the PLL with a raw measurement of the difference between the actual carrier phase and that of a reconstruction of the signal that exists in the PLL's numerically controlled oscillator (NCO). As illustrated in the figure, the raw phase difference measurement, $\Delta\phi_{meas}$, is the angle between the +*I* axis and the vector from the origin to the [*I*;*Q*] point.

If the PLL were tracking the signal perfectly and if there were no thermal noise or scintillation-induced amplitude and phase variations, then each red cloud of points on each of the two plots would collapse into a single point. These points would lie along the Q axis in the PLL implementations whose data are plotted in Fig. 3. Thermal noise causes the points to spread out into a cloud. Amplitude scintillation causes power fades, which appear on the [*I*;*Q*] plane as elongation of the clouds in the direction of the origin because amplitude is proportional to the distance of the cloud from the origin and power is proportional to the distance squared. The presence of navigation data bits with a Binary Phase-Shift Keying (BPSK) modulation causes the [*I*;*Q*] points to split into 2 clouds on the left-hand L1 C/A signal plot. There is only 1 cloud on the right-hand L2C CL plot because the CL signal does not carry data bits.

Given these facts, it is straightforward to understand why the L2C CL signal has an advantage in scintillation tracking in comparison to the L1 C/A signal. Each of the signals has a 360 deg carrier phase ambiguity because a 1-cycle phase error has no effect on the location of a measured [*I*;*Q*] point on Fig. 3. The L1 C/A signal also has a 180 deg phase ambiguity because a half-cycle phase error has exactly the same effect on an [*I*;*Q*] point as does a change of sign of a +1/-1 navigation data bit. A PLL that tracks an L1 C/A signal must use the horizontal blue line in the left-hand plot of Fig. 3 in order to distinguish which of the two possible point clouds is the cloud from which a particular [*I*;*Q*] pair has been sampled.

These two point clouds move towards the origin and intersect during the deep power fades of strong scintillations. As they approach the origin, the phase error standard deviation of each measurement increases because the aspect ratio of the cloud width divided by its distance from the origin increases. When the two clouds contact, the PLL will start to make errors in its association of [*I*;*Q*] pairs with clouds, that is, with data bit values. These mis-associations correspond to 180 deg phase measurement errors. If enough errors of this type occur, then the tracking loop will start to slip half cycles, and eventually it will completely lose carrier lock.

The L2C CL signal, on the other hand, has no such problem of deciding between two point clouds. Therefore, it does not need to make a bit decision along

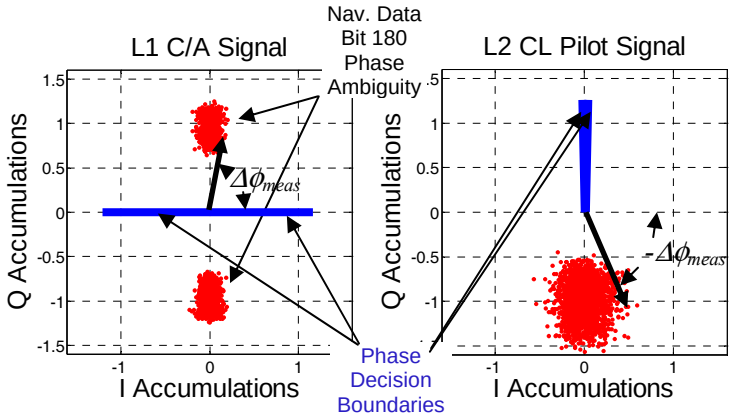

Fig. 3. Comparison of carrier phase measurements from [I;Q] accumulations for L1 C/A signal (left-hand plot) and for L2 CL signal (right-hand plot).

the horizontal axis of the [*I*;*Q*] plane. The only decision that it must make is whether a full cycle slip has occurred. This amounts to a decision at the vertical blue pair of line segments that bracket the vertical +Q axis on the right-hand plot of Fig. 3. This ambiguity is inherent in all phase detectors because of the fact that one carrier cycle looks like the next.

In the final analysis, the presence of data bits means that the PLL starts to have significant problems when the two [*I*;*Q*] clouds approach close enough to the origin to cause the phase measurement error standard deviation to be a significant fraction of 90 deg. If using a pilot signal, on the other hand, then problems occur only when the error standard deviation becomes a significant fraction of 180 deg. Thus, a PLL for a pilot signal will track more robustly during scintillation-induced power fades than will a PLL for a signal that carries data bits.

III. A KALMAN-FILTER-BASED PLL FOR TRACKING THE L2 CL SIGNAL

A. Kalman Filter Equations for CL Signal PLL

The PLL that has been developed for tracking the L2C CL signal is a modified form of the Kalman-filter-based PLLs that were originally introduced in Refs. 16 and 17. The Kalman filter estimates the following state vector at the accumulation start/stop time t_k:

$$\boldsymbol{x}_k = [\Delta\phi_k, \omega_k, \alpha_k]^{\mathrm{T}} \quad (1)$$

where $\Delta\phi_k$ is the difference between the true carrier phase and the phase of the PLL's NCO, ω_k is the carrier Doppler shift, and α_k is the rate of change of carrier Doppler shift.

The Kalman filter PLL works from sample to sample, and its operations can be defined by considering a single accumulation/sample interval that starts at time t_k and that ends at time t_{k+1}. At the start of this interval, the Kalman filter begins with its *a posteriori* estimates of the states:

$$\hat{\boldsymbol{x}}_k = [\Delta\hat{\phi}_k, \hat{\omega}_k, \hat{\alpha}_k]^{\mathrm{T}} \quad (2)$$

The qualifier "*a posteriori*" indicates that these estimates are based on all accumulation data that have been measured up to, but not beyond, time t_k. The latest such data that will have been used are the accumulations I_k and Q_k, which will have been computed during the sample interval from t_{k-1} to t_k.

The Kalman filter's first operation is the following dynamic propagation from time t_k to time t_{k+1}:

$$\begin{bmatrix} \Delta\bar{\phi}_{k+1} \\ \bar{\omega}_{k+1} \\ \bar{\alpha}_{k+1} \end{bmatrix} = \begin{bmatrix} 1 & \Delta t_k & 0.5\Delta t_k^2 \\ 0 & 1 & \Delta t_k \\ 0 & 0 & 1 \end{bmatrix} \begin{bmatrix} \Delta\hat{\phi}_k \\ \hat{\omega}_k \\ \hat{\alpha}_k \end{bmatrix} + \begin{bmatrix} -\Delta t_k \\ 0 \\ 0 \end{bmatrix} \omega_{PLLk} \quad (3)$$

where $\Delta t_k = t_{k+1} - t_k$ is the accumulation interval and where ω_{PLLk} is the rough Doppler shift estimate that the PLL sends to its carrier NCO during this interval. Note that ω_{PLLk} does not necessarily equal the Doppler shift estimate $\hat{\omega}_k$. In fact, there is a considerable degree of latitude in the choice of ω_{PLLk}. A particular method for choosing ω_{PLLk} will be defined below. The resulting *a priori* state estimate at time t_{k+1} is

$$\bar{\boldsymbol{x}}_{k+1} = [\Delta\bar{\phi}_{k+1}, \bar{\omega}_{k+1}, \bar{\alpha}_{k+1}]^{\mathrm{T}} \quad (4)$$

where the qualifier "*a priori*" indicates that this estimate is based on accumulation data only up through time t_k, i.e., only on data up through I_k and Q_k.

The Kalman filter finishes its operations for the interval by applying a measurement update. This update is based on the accumulations I_{k+1} and Q_{k+1}, which will have been computed by the receiver's baseband digital processor. In addition to a carrier NCO and a baseband mixer, the baseband processor will use a code chipping rate from a DLL as the input to its code NCO, which will produce the replica PRN code that the processor will use to wipe the code off of the received signal before computing its accumulations. This analysis presumes that the DLL and the code NCO perform PRN code removal with negligible error. The accumulations I_{k+1} and Q_{k+1} are used in a discriminator-like calculation in order to compute the phase measurement:

$$y_{k+1} = -atan2(Q_{k+1}, I_{k+1}) \quad (5)$$

where *atan2*(,) is the usual 2-argument arctangent function that produces outputs in the range $-\pi \le y_{k+1} \le \pi$. This measurement has a 2π phase ambiguity that is dealt with at a later stage of processing.

The Kalman filter measurement update uses an *a priori* estimate of what the measurement would have been if the state estimates had been correct. This estimate takes the form

$$\bar{y}_{k+1} = [1, \Delta t_k/2, \Delta t_k^2/6] \begin{bmatrix} \Delta\hat{\phi}_k \\ \hat{\omega}_k \\ \hat{\alpha}_k \end{bmatrix} - (\Delta t_k/2)\omega_{PLLk} \quad (6)$$

The formula in Eq. (6) represents the error between the true carrier phase and the PLL NCO's phase averaged over the interval from t_k to t_{k+1}. This formula for the average presumes an underlying continuous-time model in which $(\omega - \omega_{PLLk})$ is the time derivative of $\Delta\phi$, α is the time derivative of ω, and ω_{PLLk} is a constant.

The measurement update finishes by computing the error between y_{k+1} and $\bar{y}_{k+1}$ and by using this error in a feedback update that forms the *a posteriori* state estimate at time t_{k+1}. This error is called the filter innovation:

$$\nu_{k+1} = y_{k+1} - \bar{y}_{k+1} \quad (7)$$

The final update equation takes the form:

$$\begin{bmatrix} \Delta\hat{\phi}_{k+1} \\ \hat{\omega}_{k+1} \\ \hat{\alpha}_{k+1} \end{bmatrix} = \begin{bmatrix} \Delta\bar{\phi}_{k+1} \\ \bar{\omega}_{k+1} \\ \bar{\alpha}_{k+1} \end{bmatrix} + L\{\nu_{k+1} - 2\pi\, round(\nu_{k+1}/2\pi)\} \quad (8)$$

where L is the 3x1 Kalman filter gain matrix.

The computation in Eq. (8) that involves the innovation ν_{k+1} in the *round* operation constitutes the Kalman filter's method of dealing with the 2π phase ambiguity of the *atan2*(,) function in Eq. (5). This operation assigns a value to the phase ambiguity based on the assumption that the true measurement innovation should not lie outside the range: $-\pi \le \nu_{k+1} \le \pi$. This is a reasonable assumption given that $\bar{y}_{k+1}$ constitutes the Kalman filter's best estimate of what y_{k+1} should be.

The inclusion of this round operation tends to give the Kalman filter more tracking robustness than it would have if it were to feed back the output of the *atan2*(,) function as a simple PLL discriminator. The added robustness comes from the fact that the 2π ambiguity folding point effectively moves about in the [*I*;*Q*] plane in a way that keeps it opposite to the current best estimate of where the [*I*;*Q*] accumulations should be falling, i.e., opposite to the cloud shown in the right-hand plot of Fig. 3. This fact allows the Kalman filter's performance to be largely insensitive to the structure and bandwidth of the somewhat arbitrary feedback control law that determines

ω_{PLLk}. In a more traditional PLL, on the other hand, an improperly tuned loop filter might drive ω_{PLLk} in a way that allowed the π ambiguity folding point to get too near to the actual carrier phase, which could lead to nonlinear stability problems and eventual loss of frequency lock.

The total carrier phase estimate of this Kalman filter is the sum of the phase error estimate $\Delta\hat{\phi}_k$ and the phase of the PLL's NCO, ϕ_{PLLk}. This total phase is the receiver's estimate of the integrated Doppler shift, which equals the negative of the accumulated delta range measured in radians of carrier wavelengths. The NCO phase is the time integral of the PLL Doppler shift:

$$\phi_{PLL(k+1)} = \phi_{PLLk} + \Delta t_k \omega_{PLLk} \tag{9}$$

The total phase estimate $\Delta\hat{\phi}_k + \phi_{PLLk}$ tends to be more accurate than the PLL output ϕ_{PLLk} alone even if $\Delta\phi_k$ is relatively small. Similarly, the state estimate $\hat{\omega}_k$ is normally a more accurate estimate of the carrier Doppler shift than is ω_{PLLk}.

This Kalman filter effectively implements a 3rd-order PLL through its use of 3 states. As is usual with a 3rd-order PLL, it can track a ramping Doppler shift with zero phase error. That is, it can deal with a non-zero constant phase acceleration α in a way that results in zero bias in the total phase estimate $\Delta\hat{\phi}_k + \phi_{PLLk}$.

The Kalman filter implemented in Eqs. (3), (5), (6), (7), and (8) represents a straightforward application of Kalman filter theory for the chosen system model. References 18 and 19 are text books that explain Kalman filter theory well.

B. A Stabilizing Feedback to Drive the Carrier NCO

The choice of carrier NCO frequency ω_{PLLk} is somewhat arbitrary. It must not differ from the true Doppler shift by a large enough amount to cause aliasing or even to cause significant power loss in the accumulations.

A variety of stabilizing feedback control laws could be used in order to synthesize ω_{PLLk} based on the state estimates. The only restriction is that the state estimates $\Delta\hat{\phi}_k$, $\hat{\omega}_k$, and $\hat{\alpha}_k$ cannot be used to compute the NCO frequency for accumulation index values less than k+1. This restriction ensures that the Kalman filter can be implemented in real-time. The final dynamic propagation and measurement update that are used to form the estimates in $\Delta\hat{\phi}_k$, $\hat{\omega}_k$, and $\hat{\alpha}_k$ cannot be completed until after time t_k because the measurement update requires the accumulations I_k and Q_k, which become available only after time t_k. Presuming that the processor is fast enough to perform the computations in Eqs. (3-8) in less than one accumulation interval, it is possible to use $\Delta\hat{\phi}_k$, $\hat{\omega}_k$, and $\hat{\alpha}_k$ in order to compute $\omega_{PLL(k+1)}$ in real-time, i.e., before time t_{k+1}, at which point this quantity is needed by the carrier NCO.

The NCO feedback control law that has been used in the present study takes the form [16]:

$$\begin{aligned}\omega_{PLL(k+1)} = \frac{1}{\Delta t_{k+1}}\{&(1-\eta)^2(\Delta\hat{\phi}_k - \Delta\phi_{des}) \\ &+ (1-2\eta)\Delta t_k(\hat{\omega}_k - \omega_{PLLk}) - \eta\Delta t_k^2\hat{\alpha}_k\} \\ &+ \hat{\omega}_k + \frac{(\Delta t_k + \Delta t_{k+1})^2}{2\Delta t_{k+1}}\hat{\alpha}_k\end{aligned} \tag{10}$$

where η is a feedback tuning parameter and $\Delta\phi_{des}$ is the desired steady-state value of the phase error $\Delta\phi_k$. As a point of reference, this steady-state target value was arbitrarily set to $\Delta\phi_{des} = -\pi/2$ in the PLL that generated the data for the right-hand plot of Fig. 3. This feedback control law has been designed in order to make the NCO phase error dynamics obey the following stable 2nd-order linear difference equation in the absence of noise or other disturbances:

$$\Delta\hat{\phi}_{k+2} - 2\eta\Delta\hat{\phi}_{k+1} + \eta^2\Delta\hat{\phi}_k = (1-\eta)^2\Delta\phi_{des} \tag{11}$$

This fact can be proved by a set of algebraic manipulations that use Eqs. (3) and (10) and that assume that the *a posteriori* and *a priori* state estimates are equal. The two characteristic values of the dynamic model in Eq. (11) are η repeated twice. Thus, these error dynamics will be stable for any tuning value in the range $-1 < \eta < 1$. Typically one uses positive values for η that are near 1 in order to have a low bandwidth. Note, however, that the bandwidth of this NCO error dynamics model is completely decoupled from the bandwidth of the Kalman filter.

Although not used in the present study, it should be acceptable to use a simple frequency-lock loop (FLL) in order to compute $\omega_{PLL(k+1)}$. The following FLL feedback control law should work satisfactorily:

$$\omega_{PLL(k+1)} = \hat{\omega}_k + (\Delta t_k + \tfrac{1}{2}\Delta t_{k+1})\hat{\alpha}_k \tag{12}$$

In this case, the carrier phase estimate $\Delta\hat{\phi}_k + \phi_{PLLk}$ still should be a very good phase estimate, like that of any good PLL, even though the estimate ϕ_{PLLk} would tend to be a very poor estimate due to drift between the NCO phase and the true phase. The Kalman filter would accumulate an accurate estimate of this drift in its $\Delta\hat{\phi}_k$ state.

C. Tuning of the Kalman Filter

Implementation of the PLL Kalman filter requires knowledge of the 3x1 filter gain matrix L. One could choose to implement a time-varying Kalman filter in

which L varied with the sample index k to become L_k. Such an implementation would necessitate the use of an estimation error covariance propagation and a gain computation for each accumulation interval [18,19].

A time-varying gain computation could adapt the filter to deal with the increased phase error measurement standard deviation that occurs when scintillations cause the power to fade, but this is not the only important issue. A truly optimal implementation would require an additional adaptation parameter that accounted for the increased rapidity of the carrier phase changes that occurred during canonical fades. The increased measurement noise during fades would tend to decrease the magnitudes of the gain elements in L_k, but the increased phase dynamics uncertainty would tend to increase these magnitudes.

Therefore, it is reasonable to attempt to use a fixed-gain Kalman filter. A further advantage of a fixed-gain filter is its elimination of the expensive matrix computations that are used by a time-varying filter in order to manipulate the error covariance matrix and in order to compute the gain matrix.

Fixed-gain filters occur in steady-state when the dynamics model is time-invariant. If one presumes a nominal value of the accumulation interval $\Delta t_k = \Delta t$ independent of k, then one can compute a fixed filter gain. This is what has been done. As a further simplification, a limiting property of the Kalman filter has been used in order to allow the steady-state gain to be computed using the pole placement technique. This known property is that the filter's characteristic values tend towards a Butterworth pattern. Therefore, the steady-state gain matrix L has been chosen so that the filter's steady-state error state transition matrix

$$\Phi_{cl} = \begin{bmatrix} 1 & \Delta t & 0.5\Delta t^2 \\ 0 & 1 & \Delta t \\ 0 & 0 & 1 \end{bmatrix} - L[1,\ \Delta t/2,\ \Delta t^2/6] \qquad (13)$$

will have the desired closed-loop eigenvalues $exp(-2\pi B_{PLL}\Delta t)$, $exp([-1+j\sqrt{3}\,]\pi B_{PLL}\Delta t)$, and $exp([-1-j\sqrt{3}\,]\pi B_{PLL}\Delta t)$, where B_{PLL} is the bandwidth of the Kalman filter in Hz and Δt is given in seconds.

The results section of this paper considers PLLs that all use the same value for the nominal accumulation period, but it considers two different possible Kalman filter tunings. The nominal accumulation period has been chosen to be Δt = 0.010 sec, which yields a 100 Hz accumulation frequency. This interval has been found to yield good tracking results in strong equatorial scintillations [11]. The two gain matrices that have been considered along with their corresponding filter bandwidths are:

$$L = \begin{bmatrix} 0.291004 \\ 4.391752 \\ 33.123850 \end{bmatrix} \quad \text{for } B_{PLL} = 2.5 \text{ Hz} \qquad (14a)$$

$$L = \begin{bmatrix} 0.943983 \\ 50.129594 \\ 1323.319695 \end{bmatrix} \quad \text{for } B_{PLL} = 10 \text{ Hz} \qquad (14b)$$

The 10 Hz bandwidth tuning in Eq. (14b) has been considered because this bandwidth has been found to be good for traditional PLLs when operating in equatorial scintillations [11]. The lower bandwidth of 2.5 Hz in Eq. (14a) has been considered because the robustness of the proposed Kalman-filter-based PLL may depend significantly on its bandwidth, and the optimal bandwidth may differ from that determined in Ref. 11 for traditional PLLs. The consideration of an alternate bandwidth provides a means of probing this issue. In fact, several additional bandwidths have been considered, but only these two are reported here because the results concentrate on these two tunings and because these two cases serve to illustrate how tuning is accomplished.

For completeness sake, the tuning of the ad hoc ω_{PLL} feedback law in Eq. (10) is also presented. The tuning value η = 0.774597 has been chosen. This yields a bandwidth of $-ln(\eta)/(2\pi\Delta t)$ = 4.065 Hz. Note that the Kalman filter masks the effects of this feedback from its estimation process. Therefore, the bandwidth of this ad hoc feedback law in no way influences the effective bandwidth of the Kalman-filter-based PLL.

D. Variant Kalman Filter for L1 C/A Tracking

This study also considers a PLL for tracking the L1 C/A signal in order to provide a point of comparison for the L2C CL signal PLL. The L1 C/A PLL is almost the same as the Kalman-filter-based PLL described earlier in this section, except that it includes some extra steps in order to wipe the data bits off of the signal before computing the measurement y_k. These steps constitute its method for making the decision about the point cloud to which a particular $[I;Q]$ sample belongs, as in the left-hand plot of Fig. 3.

This PLL makes the assumption that the carrier tracking loop has achieved bit synchronization so that each bit period corresponds exactly to an integer number of accumulation periods. The bit period is nominally 0.020 sec long, and it can vary slightly due to Doppler shift. Therefore, the nominal accumulation period is Δt_k = 0.020/K seconds, where K is the integer number of accumulations per bit. Without loss of generality, suppose that the accumulation indices have been lined up with the bit periods so that the first bit period consists of accumulations k = 0, 1, 2, ..., K-1, the second bit period consists of accumulations k = K, K+1, K+2, ... 2K-1, and the m^{th} bit period consists of accumulations (m-1)K, (m-1)K+1, (m-1)K+2, ..., mK-1.

The L1 C/A signal PLL makes its decisions about the data bits' signs by using an adaptation of the dot-product bit detection scheme described in Ref. 11. The basic idea is to accumulate the I_k and Q_k values over as much of the current bit interval as has elapsed and to use these accumulations in order to decide on the bit sign. In Ref. 11, the method of deciding the bit sign is to form the dot product of the current partial-bit-length accumulations of I_k and Q_k with the full-bit-length accumulations from the previous bit interval. If this dot product is positive, then the current bit is assigned the same value as the previous bit. If the dot product is negative, then the bit sign is reversed from the previous bit. The reason for using this strategy is that the longer accumulations of I_k and Q_k, up to K of them summed together, provides an increased signal-to-noise ratio (SNR) and, therefore, a decreased probability of bit detection error.

The use of a Kalman filter PLL affords the opportunity to construct an improved version of the dot-product method of Ref. 11. This improved method forms the dot product between the current partial-bit-length accumulations of I_k and Q_k and the Kalman filter's estimates of what the normalized versions of these accumulations should be. This approach has the advantage of eliminating the possibility of a bit detection error due to $\Delta\phi_k$ phase rotation between the preceding data bit interval and the current data bit interval.

The explicit formulas used for bit detection are as follows. The partial I_k and Q_k accumulations for the current bit interval are:

$$I_{bitk} = \sum_{i=K\,floor(k/K)}^{k} I_i \tag{15a}$$

$$Q_{bitk} = \sum_{i=K\,floor(k/K)}^{k} Q_i \tag{15b}$$

where the *floor*() function rounds its input argument to the nearest integer in the direction of $-\infty$. This partial bit accumulation is for navigation data bit $m = floor(k/K) + 1$. The partial accumulations for the Kalman filter's estimates of the normalized I_k and Q_k values are

$$\bar{I}_{bitk} = \sum_{i=K\,floor(k/K)}^{k} cos(\bar{y}_i) \tag{16a}$$

$$\bar{Q}_{bitk} = -\sum_{i=K\,floor(k/K)}^{k} sin(\bar{y}_i) \tag{16b}$$

where $\bar{y}_i$ is the filter's *a priori* prediction of the carrier phase measurement, as in Eq. (6). Note that the 4 partial-bit accumulations can be constructed recursively by using the following formulas:

$$I_{bitk} = \begin{cases} I_k & \text{if } K\,floor(k/K) = k \\ I_{bit(k-1)} + I_k & \text{if } K\,floor(k/K) < k \end{cases} \tag{17a}$$

$$Q_{bitk} = \begin{cases} Q_k & \text{if } K\,floor(k/K) = k \\ Q_{bit(k-1)} + Q_k & \text{if } K\,floor(k/K) < k \end{cases} \tag{17b}$$

$$\bar{I}_{bitk} = \begin{cases} cos(\bar{y}_k) & \text{if } K\,floor(k/K) = k \\ \bar{I}_{bit(k-1)} + cos(\bar{y}_k) & \text{if } K\,floor(k/K) < k \end{cases} \tag{17c}$$

$$\bar{Q}_{bitk} = \begin{cases} -sin(\bar{y}_k) & \text{if } K\,floor(k/K) = k \\ \bar{Q}_{bit(k-1)} - sin(\bar{y}_k) & \text{if } K\,floor(k/K) < k \end{cases} \tag{17d}$$

The 4 partial-bit accumulations in Eqs. (17a)-(17b) are used in the following dot product rule in order to estimate the sign of the current navigation data bit:

$$\bar{d}_{bitk} = \begin{cases} +1 \text{ if } 0 \le (I_{bitk}\bar{I}_{bitk} + Q_{bitk}\bar{Q}_{bitk}) \\ -1 \text{ if } (I_{bitk}\bar{I}_{bitk} + Q_{bitk}\bar{Q}_{bitk}) < 0 \end{cases} \tag{18}$$

Given the bit estimate from Eq. (18), but for accumulation k+1, the Kalman filter computes its carrier phase measurement by using the following modified form of Eq. (5):

$$y_{k+1} = -atan2([\bar{d}_{bit(k+1)}Q_{k+1}],[\bar{d}_{bit(k+1)}I_{k+1}]) \tag{19}$$

The Kalman filter PLL uses this modified measurement computation along with Eqs. (3), (6), (7), (8), and (10) in order to implement its computations for one accumulation interval. Thus, it operates exactly like the L2C CL PLL after it has wiped the navigation data bit off of its accumulations using Eqs. (17a)-(19).

This PLL forms K different estimates of the navigation data bit that applies for the m^{th} bit interval, $\bar{d}_{bit([m\text{-}1]K)}$, $\bar{d}_{bit([m\text{-}1]K+1)}$, $\bar{d}_{bit([m\text{-}1]K+2)}$, ..., $\bar{d}_{bit(mK\text{-}1)}$. The best estimate is the final one, $\bar{d}_{bit(mK\text{-}1)}$; it is based on accumulation sums, as in Eqs. (16a) and (16b), that have the highest SNR. This final estimate should be used as the navigation data bit if the receiver needs to recover the navigation message.

E. Variant Kalman Filter for Semicodeless P(Y) Tracking of L2 Signal

A Kalman-filter-based PLL has also been designed for semicodeless P(Y) tracking of the L2 signal. This PLL provides a comparison case that should be representative of the capabilities of current state-of-the-art civilian dual-frequency receivers.

The PLL for the L2 P(Y) signal is exactly like the PLL for the L2C CL signal except for manner in which its baseband processor computes the accumulations I_k and Q_k. An L2C CL receiver computes these accumulations by using a DLL and a code NCO in order to produce a reconstruction of the known CL PRN code, which it uses

to wipe the PRN code off of the signal before the carrier NCO mixes the signal to baseband and before the summation of the accumulations.

For semicodeless P(Y) tracking, the full P(Y) code is not available. A semicodeless receiver uses an approximate reconstruction of the P(Y) code in place of the true P(Y) code in order to do code wipe-off, but it otherwise functions like any other receiver. Its code reconstruction takes the form:

$$Y(t) = P(t)\hat{W}(t) \tag{20}$$

where $Y(t)$ is the unknown $P(Y)$ code, $P(t)$ is the known P code [12], and $\hat{W}(t)$ is the estimated time history of the unknown encryption chips that turn the P code into the P(Y) code. These encryption chips have an average chipping rate of 480 KHz, and they have a known timing relative to the P code [20]. The only unknown is the proper sequence of the actual +1/-1 chip values. A semicodeless receiver constructs estimates of the $W(t)$ chips by using the L1 signal. In one of the best semicodeless methods, the method known as soft decision Z-tracking, the estimate of $W(t)$ is constructed as follows [15]:

$$\hat{W}(t) = \sum_{n=-\infty}^{\infty} \hat{W}_n \Pi_{\delta t_n}(t-t_n) \tag{21}$$

where the function $\Pi_{\delta t}(t)$ is the usual rectangular support function, which is equal to one over the interval $0 \le t < \delta t$ and zero elsewhere. $\hat{W}_n$ is the "soft" estimate of the n^{th} W-code chip. The interval from t_n to t_{n+1} $(=t_n+\delta t_n)$ is the nominal broadcast interval of encryption chip W_n. The chip estimate is constructed from the L1 signal as follows

$$\hat{W}_n = \int_{t_n-\hat{\tau}_{L1}}^{t_{n+1}-\hat{\tau}_{L1}} z_{L1}(t)\, sin[\omega_{L1}t + \hat{\phi}_{L1}(t)]P(t-\hat{\tau}_{L1})dt \tag{22}$$

The integration interval is the chip's nominal broadcast interval offset by $\hat{\tau}_{L1}$, which is the receiver DLL's estimate of the L1 P(Y) code transmission delay. This code delay estimate is derived using the L1 C/A code and the known timing relationship between the C/A and P(Y) codes on L1. The function $z_{L1}(t)$ is the received L1 signal, and $sin[\omega_{L1}t + \hat{\phi}_{L1}(t)]$ is the L1 PLL's estimate of the quadrature component of the received L1 carrier signal.

This method of estimating the W_n encryption chips is termed "soft" because the $\hat{W}_n$ values are allowed to take on a range of real values; they are not forced to be either +1 or -1. This approach effectively weights the certainty of the knowledge of the $\hat{W}_n$ chip's sign by the amplitude of the chip, which is a reasonable thing to do given the typically low SNR of the $\hat{W}_n$ estimate.

The chip estimation formula in Eq. (22) fails to account for the possible effects of code Doppler shift. The generalization to handle code Doppler shift is fairly straightforward, but has been omitted in order to simplify the presentation.

The semicodeless P(Y) PLL does not have to deal with uncertainty about the 50 Hz navigation data bits. This is true because the data bits are normally broadcast on both the L1 and L2 channels. Therefore, the $\hat{W}_n$ encryption chip estimate already has an estimate of the current navigation data bit factored into it, and the use of the approximate P(Y) replica signal in Eq. (20) to wipe the PRN code off of the received L2 signal has the effect of also wiping off the navigation data bits.

IV. COLLECTION AND PROCESSING OF DUAL-FREQUENCY SCINTILLATION DATA

A. Collection of Equatorial Scintillation Data

Wide-band dual-frequency scintillation data were collected in Natal, Brazil in January of 2007. In this context, wide-band data refers to the digitized outputs of an RF front-end that has a wide enough filter bandwidth and a fast enough sampling rate to capture all of the main power lobe of the PRN code in question.

The wide-band scintillation data have been collected using the dual-frequency RF front-end that is depicted in Fig. 4. This front-end is based on the Zarlink/Plessey GP2015 front-end for the L1 signal. The dual-frequency front-end uses two GP2015 chips. One is connected directly to the output of the antenna/preamp through a splitter, and it digitizes the L1 C/A code band with a final filter bandwidth of 1.9 MHz and a sampling rate of 5.7143 MHz, which ensures that the 2.046 MHz wide main lobe of the C/A signal is captured. The other GP2015 receives the L2 signal after it is filtered and then mixed with a 347.8261 MHz signal in order to bring its frequency near to L1. Its final bandwidth and sampling frequency are the same as for the L1 channel, which ensures that the 2.046 MHz wide main lobe of the L2C signal is captured. The L2 to L1 mixer, both GP2015 mixing chains, and both GP2015 sample clocks are referenced to a common 10 MHz oscillator in order to ensure phase coherence. Reference 21 contains additional information about this dual-frequency RF front-end.

The outputs from the dual-frequency RF front-end were sent to a computer through a digital data acquisition card, and they were stored on disk. The data recording computer was controlled by an operator who also had access to a real-time scintillation monitor. The real-time monitor provided the operator with a means of assessing whether significant scintillations were occurring. Wide-band data were retained only for time periods that showed

significant levels of scintillation.

The advantage of collecting wide-band data is that the data are guaranteed to retain all of their information about scintillations. A wide-band data recorder does not use a PLL or a DLL to track the signal in order to remove the carrier or the PRN code because the wide-band data has enough room in its spectrum to retain these signal features. Therefore, it is impossible to lose the signal due to loss of lock in a tracking loop.

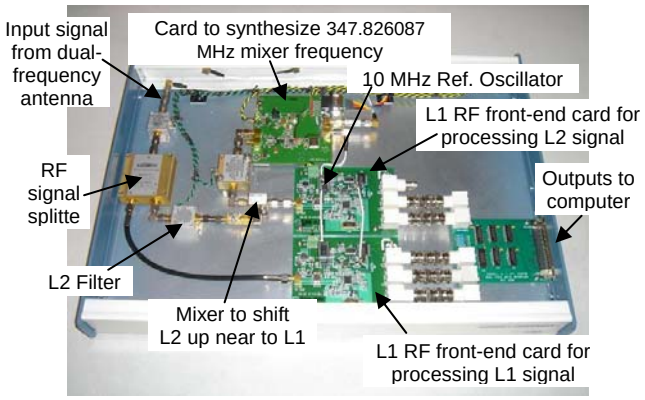

Fig. 4. RF front-end of a dual-frequency digital storage receiver for the L1 C/A and L2C signals.

Wide-band dual-frequency scintillation data were recorded for the GPS signal PRN 12 on the evenings of Jan. 17 and Jan. 20, 2007. The entire data recording campaign lasted from Jan. 13-24, 2007, but scintillations occurred on PRN 12 only on these two evenings.

Only three GPS satellites were sufficiently modern in January 2007 to be broadcasting the L2C signal. GPS satellites broadcast this signal if they are from Block IIR-M, Block IIF, or beyond. The three orbiting Block IIR-M satellites were PRN 12, 17, and 31. Of these three, only PRN 12 and 17 were visible from Natal, Brazil after local sunset, which is the time when scintillations occur. The line-of-sight (LOS) vector to PRN 17 never passed through a scintillating portion of the ionosphere during the campaign.

It was disappointing to get scintillations only on one dual-frequency signal, but this was better than the outcome of a similar campaign in Jan. 2006, when only PRN 17 was broadcasting the L2C signal and when its LOS vector never passed through scintillations. Future scintillation data collection campaigns are expected to yield richer sets of dual-frequency data as additional L2C-capable GPS satellites get launched and as the next solar maximum approaches.

B. MATLAB Post-Processing of Wide-band Scintillation Data

The wide-band data were post-processed in a MATLAB software receiver in order to evaluate the performance of the PLL tracking loops that have been discussed in Section III. Figure 5 presents a block diagram for this post-processing scenario. The left-hand side of the block diagram defines the data collection hardware, and the right-hand side depicts the MATLAB software receiver.

The purpose of the MATLAB software receiver is to test the Kalman-filter-based PLL in the blue-outlined block on the extreme right-hand side of Fig. 5's second line. This block exactly implements the PLL algorithm of Section III. The many additional blocks shown in the diagram are needed in order to test the PLL using real data.

The signal acquisition procedure uses FFT block processing, as in Refs. 22 and 23, in order to get initial estimates of the PRN code offsets and carrier Doppler shifts of the L1 C/A signal and the L2C CM signal. The acquisition of the L2C CM signal uses the Doppler shift estimate from the L1 C/A signal in order to reduce its Doppler search space. The L2C CL signal is acquired by considering all 75 possible offsets of the CL code start time relative to the CM code start time; the repeat period of the CM code is 0.020 sec, and the repeat period of the CL code is 1.5 seconds [12]. A small number of fractional code chip offsets of the CL code relative to each of the 75 possible offsets with respect to the CM code are used to

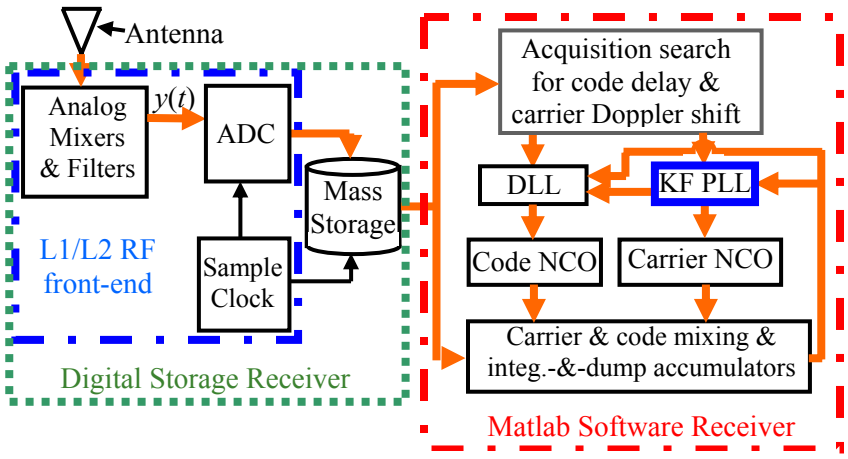

Fig. 5. Block diagram of wide-band data collection and off-line processing in a MATLAB software receiver.

compute CL accumulations, and the offset with the largest accumulation power determines the CL code start time. Visual inspection of the CL code correlation as a function of PRN code offset has been used in order to verify the presence of the expected triangular peak.

The completed acquisition calculations are used to initialize the DLL's code phase estimate and the PLL's

carrier Doppler shift estimate, $\hat{\omega}_0$. The PLL's first two NCO frequencies, ω_{PLL0} and ω_{PLL1} are also initialized using the acquisition's Doppler shift estimate. The PLL's carrier NCO phase is initialized to the value $\phi_{PLL0} = 0$, and its Kalman filter phase error estimate is initialized using the first accumulations: $\Delta\hat{\phi}_0 = -atan2(Q_0, I_0)$. The PLL's carrier Doppler shift rate estimate is initialized to $\hat{\alpha}_0 = 0$.

The DLL uses a standard first-order loop that includes carrier aiding. It uses a non-coherent dot-product discriminator with a ½ chip early/late spacing. The discriminator includes both a power normalization in order to maintain bandwidth during canonical fades and an upper magnitude bound of ¼ chip in order to limit the effects of noise during the deepest fades. DLL bandwidths in the range 0.2 to 0.3 Hz have been used in this study.

The prompt I_k and Q_k accumulations that are used by the PLL are computed in the lower block of the MATLAB software receiver. This block performs its code mixing, carrier baseband mixing, and integrate-and-dump calculations according to the following formulas

$$I_k = \sum_{i=i_k}^{i_{k+1}-1} z(\tau_i)\cos[\omega_{IF}\tau_i + \phi_{PLLk} + \omega_{PLLk}(\tau_i - t_k)] \times C[\frac{f_{ck}}{f_{cnom}}(\tau_i - t_k) + t_{nomk}] \quad (23a)$$

$$Q_k = \sum_{i=i_k}^{i_{k+1}-1} z(\tau_i)\sin[\omega_{IF}\tau_i + \phi_{PLLk} + \omega_{PLLk}(\tau_i - t_k)] \times C[\frac{f_{ck}}{f_{cnom}}(\tau_i - t_k) + t_{nomk}] \quad (23b)$$

where $z(\tau_i)$ is the output signal of the RF front-end at sample time τ_i, and i_k is the index of the first sample in the accumulation interval; it is the minimum value of i such that $\tau_i \geq t_k$. The quantity ω_{IF} is the signed nominal intermediate frequency of the carrier signal at the output of the RF front-end -- it is negative if the RF front-end uses high side mixing. The function $C[\tau]$ is the signal's known PRN code. The quantity f_{ck} is the Doppler-shifted PRN code chipping rate as determined by the DLL, and $f_{cnom} = 1.023\text{x}10^6$ Hz is the nominal PRN code chipping rate. The quantity t_{nomk} is the nominal phase, expressed in seconds, of the point in the prompt PRN code that the DLL estimates as having been received at time t_k.

Although implemented off-line, all of the PLL, DLL, and accumulation calculations are implemented in a manner that is consistent with real-time operation, as discussed in Section III. Therefore, the performance of any given PLL in this off-line test environment will be equivalent to the performance that it could have achieved in real-time if it had been implemented in a receiver that had been operated during the scintillation data collection campaign.

V. PHYSICS-BASED SIMULATION OF PLL TRACKING DURING DUAL-FREQUENCY SCINTILLATIONS

A physics-based simulation of dual-frequency scintillations has been developed as a means of providing a rich set of test cases for the PLLs of Section III. The data from actual scintillations described in Section IV contain less than 120 minutes of L2 scintillations that have an S_4 intensity index above 0.2. Less than 20 minutes of the data have an S_4 above 0.4, and no data have an S_4 above 0.51. These do not represent challenging cases for scintillation tracking. Therefore, it was decided to develop a physics-based simulation of dual-frequency scintillations in order to be able to fully probe the PLLs' tracking robustness without having to wait for data from future scintillation monitoring campaigns.

A. Phase Screen Scintillation Model

A phase screen provides a relatively simple physical model that is deemed to have a reasonable level of validity for equatorial scintillations [13]. Using the coordinate system of Fig. 1, a phase screen model starts with a profile of the vertical total electron content as a function of horizontal displacement perpendicular to the magnetic field, $TEC(x)$. It uses $TEC(x)$ in the following formula in order to determine an x profile for the net carrier phase advance [24]:

$$\phi_{sc}(x) = (2\pi)^2\left[\frac{40.3\,TEC(x)}{c\omega}\right] \quad (24)$$

where c is the speed of light, ω is the carrier frequency, either ω_{L1} or ω_{L2}, and $TEC(x)$ is expressed in units of electrons/m^2. This phase advance profile is used to define an instantaneous phase change that occurs in the signal as it passes through the thin screen of the ionosphere at the vertical position $z = 0$. If a given signal quantity, such as voltage in the x direction, takes on the following value just above the ionosphere

$$u(x, y, 0^-, t) = A_0 e^{j\omega t} \quad (25)$$

then just below the ionosphere this same signal quantity is perturbed by the phase screen to become

$$u(x, y, 0^+, t) = A_0 e^{j\{\omega t + \phi_{sc}(x)\}} \quad (26)$$

The signal in Eq. (25) represents a plane wave of amplitude A_0 that is incident perpendicular to the ionosphere. The perturbed signal in Eq. (26) has the same amplitude just below the ionosphere, but it has a perturbed phase that varies with x.

The phase screen model propagates the phase change effects to the receiver at the ground. The propagation calculation uses the Huygens-Fresnel approximation of

Kirchhoff's integral for wave propagation from the boundary to an interior point of a defined region. The boundary of integration is the lower surface of the ionosphere, and the interior point in question is the receiver location z meters below the ionosphere. The Huygens-Fresnel formula is:

$$\begin{aligned}[\widetilde{I}_{sc}(x;\omega)+j\widetilde{Q}_{sc}(x;\omega)]e^{j\omega t} &= u(x, y, z, t) \\ &= \frac{A_0 jk}{2\pi z} e^{j(\omega t - kz)} \\ &\quad \times \int_{-\infty}^{\infty}\int_{-\infty}^{\infty} e^{j\{\phi_{sc}(x')-k[(x-x')^2+(y-y')^2]/(2z)\}} dx'\, dy' \\ &= A_0\sqrt{\frac{jk}{2\pi z}} e^{j(\omega t - kz)} \int_{-\infty}^{\infty} e^{j\{\phi_{sc}(x')-k(x-x')^2/(2z)\}} dx' \end{aligned} \quad (27)$$

where $k = \omega/c = 2\pi/\lambda$ is the signal's wave number, with λ being its wavelength. This equation's outputs, $\widetilde{I}_{sc}(x;\omega)$ and $\widetilde{Q}_{sc}(x;\omega)$, define the scintillation-induced in-phase and quadrature signal perturbations at the receiver, and they can be used to simulate the scintillations' effects on a PLL.

The in-phase and quadrature scintillation perturbations can be translated into functions of time by assuming an ionospheric drift velocity. Suppose that a "frozen" $TEC(x)$ vs. x profile drifts past the ionospheric pierce point in the x direction and that it has a drift speed of v_{drift}. Experimental results have shown that this is a reasonably accurate model for the time evolution of equatorial scintillations as sensed at a ground-based receiver [7]. Typical drift speeds are on the order of v_{drift} = 100 m/s. This drift model and the reasonable assumption that $v_{drift} << c$ can be used to define in-phase and quadrature scintillation time histories for the L1 and L2 signals: $I_{sc\mathrm{L1}}(t) = \widetilde{I}_{sc}(v_{drift}t;\omega_{\mathrm{L1}})$, $Q_{sc\mathrm{L1}}(t) = \widetilde{Q}_{sc}(v_{drift}t;\omega_{\mathrm{L1}})$, $I_{sc\mathrm{L2}}(t) = \widetilde{I}_{sc}(v_{drift}t;\omega_{\mathrm{L2}})$, and $Q_{sc\mathrm{L2}}(t) = \widetilde{Q}_{sc}(v_{drift}t;\omega_{\mathrm{L2}})$.

The phase screen model requires a method of generating a reasonable $TEC(x)$ vs. x profile and a method of evaluating the integral in Eq. (27). The $TEC(x)$ profile is determined by using a random number generator and a filter. The filter assures that $TEC(x)$ has a pre-defined spatial power spectral density (PSD) of the form:

$$S_{TT}(\Omega) = \frac{S_{TT0}\Omega_{min}^{p}}{\Omega^{p} + \Omega_{min}^{p}} \quad (28)$$

where Ω is the spatial frequency in rad/m, p is the high-frequency roll-off exponent, Ω_{min} is the break frequency that defines the boundary between a flat power spectrum at low frequency and a decreasing power spectrum at high frequency, and S_{TT0} is the low-frequency limit of the PSD. This form of PSD matches that of Ref. 13 at high frequencies if $p \cong 4$.

The Huygens-Fresnel integral in Eq. (27) can be evaluated using the Fast-Fourier Transform (FFT) algorithm if a special Fourier transform pair is used in order to exploit the transform's convolution property [14]. The needed Fourier transform pair is

$$g(x) = \sqrt{\frac{jk}{z}} e^{-jkx^2/(2z)} \quad \text{and} \quad G(\Omega) = e^{jz\Omega^2/(2k)} \quad (29)$$

where Ω is the spatial frequency argument of the Fourier transform in units of rad/m. Examination of Eq. (27) reveals that its final integral is the convolution of $g(x)$ with the function $h(x) = e^{j\phi_{sc}(x)}$. Therefore, its integral can be computed by calculating $H(\Omega)$, which is the Fourier transform of $h(x)$, forming the product $H(\Omega)G(\Omega)$, and inverse transforming the result.

The required Fourier transform and inverse Fourier transform are carried out numerically using the FFT algorithm, and the result is a set of $\widetilde{I}_{sc}(x;\omega)$ and $\widetilde{Q}_{sc}(x;\omega)$ values that are defined at a set of x grid points. A cubic spline is used in order to define $\widetilde{I}_{sc}(x;\omega)$ and $\widetilde{Q}_{sc}(x;\omega)$ for all real-valued x between the grid points, and these functions are used to define the corresponding time histories $I_{sc}(t)$ and $Q_{sc}(t)$, which are needed by the PLL simulation.

This paper's appendix documents the details of how the final $I_{sc}(t)$ and $Q_{sc}(t)$ functions are computed. It starts by showing how the $TEC(x)$ profile is generated on a set of grid of points, and it finishes by defining the cubic splines that constitute $I_{sc}(t)$ and $Q_{sc}(t)$. The appendix discusses a few subtle, but important points about how the FFT and inverse FFT (IFFT) calculations must be implemented, and it defines the underlying assumptions about $TEC(x)$ that are implied by the use of sampling and FFT calculations.

The realism of this phase screen model is illustrated by an example of its dual-frequency scintillation outputs, as shown in Fig. 6. This figure clearly shows the presence of the expected canonical fades on the L1 and L2 signals. It also shows a greater intensity of the L2 scintillations and the partial de-correlation of the L1 and L2 power fades as S_4 becomes large. Both of these phenomena are consistent with experimental observations.

B. PLL Simulation that Incorporates Phase Screen Model

The simulated $I_{sc}(t)$ and $Q_{sc}(t)$ scintillation time histories are used as inputs to the simulation of each PLL. Figure 7 depicts a block diagram of the operations that

are involved in PLL simulation. This figure shows how the phase screen scintillation model of the preceding sub-section is combined with models of accumulated delta range, L1 C/A signal navigation data bits, and receiver thermal noise in order to provide signal inputs to simulations of L1 and L2 carrier tracking PLLs. The flow of information in Fig. 7's block diagram is generally from left to right.

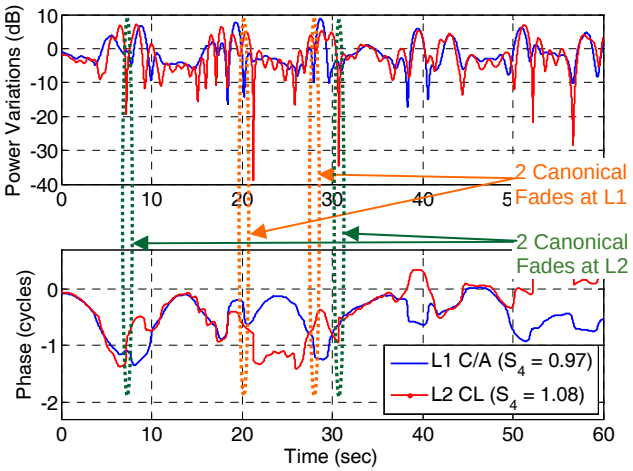

Fig. 6. Simulated L1 and L2 power (top plot) and phase (bottom plot) scintillations as generated by the phase screen model.

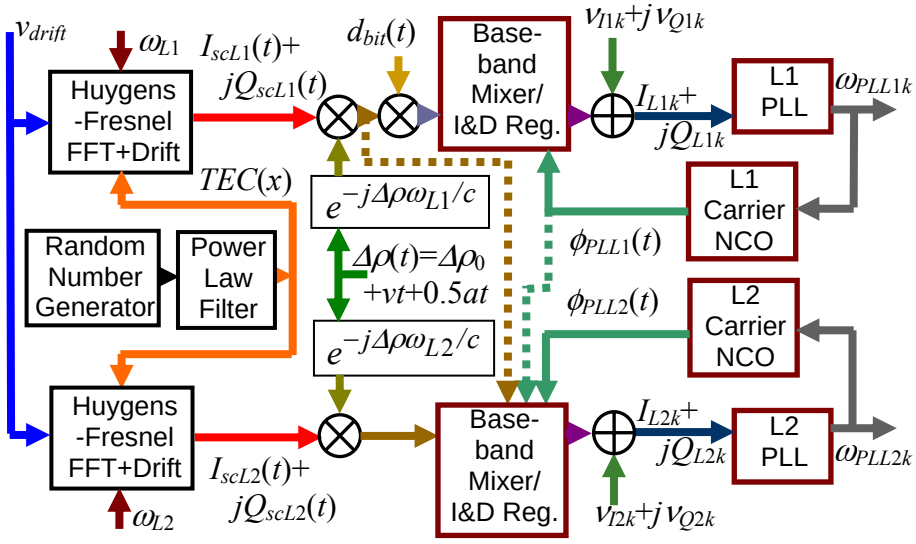

Fig. 7. Block diagram of phase screen/PLL simulation.

The 4 blocks on the extreme left-hand side of the diagram implement the phase screen simulation of the scintillations as described in the preceding subsection. The one important additional point to note about the phase screen model is that a common $TEC(x)$ density profile is generated that feeds into two Huygens-Fresnel phase screen models, one for the L1 signal and one for the L2 signal. This implies that any correlations between the L1 and L2 scintillations is firmly rooted in the physics of the phase screen model.

The outputs of the scintillation models get mixed with the accumulated delta range parts of the signals just to the left of center in the block diagram. The signal $\Delta\rho(t)$ is the accumulated delta range. It is allowed to have a non-zero initial value $\Delta\rho_0$, a non-zero initial velocity v, and a non-zero acceleration a. The delta range is scaled by the appropriate carrier frequency divided by the speed of light and is negated in order to produce the appropriate phase effect.

The L1 signal is mixed with the 50 Hz navigation data bit stream $d_{bit}(t)$. A random number generator is used to generate a random sequence of +1/-1 values at 50 Hz. The L1 PLL simulation presumes that bit lock has been achieved so that every K of its accumulation periods are aligned with a single unknown navigation data bit.

After the effects of scintillations, accumulated delta range, and L1 navigation data bits have been incorporated, the resultant signals are fed into the L1 and L2 PLLs' baseband mixers and integrate-and-dump registers. There are no PRN code mixers because this simulation makes the reasonable assumption that a good DLL is maintaining code lock and, therefore, that code wipe-off works perfectly or nearly perfectly.

The outputs of the integrate-and-dump registers are added to the noise terms v_{Ik} and v_{Qk} in order to produce the simulated I_k and Q_k accumulations. The noise is generated by a random number generator (not shown), and its covariance is sized based on the mean signal power, the mean carrier-to-noise ratio, and the accumulation interval of the integrate-and-dump register.

The I_k and Q_k accumulations are processed by the PLLs to produce the ω_{PLLk} outputs, as described in Section III of this paper, and these outputs are fed into the simulated carrier NCOs. Any reasonable real-time PLL model or even an FLL model could be substituted into this block diagram in place of the PLL models of Section III.

The carrier NCOs create the phases of the baseband mixing signals that apply during the accumulation interval from t_k to t_{k+1}: $\phi_{PLL1}(t) = \phi_{PLL1k} + \omega_{PLL1k}(t-t_k)$ and $\phi_{PLL2}(t) = \phi_{PLL2k} + \omega_{PLL2k}(t-t_k)$. These phase time histories are fed back to the blocks that simulate the baseband

mixers and the integrate-and-dump registers.

The simulation performs many of its calculations in continuous time. Continuous-time modeling starts with cubic spline models of the scintillating signals that are output by the blocks that implement the Huygens-Fresnel FFT calculations and the ionospheric drift transformation. Continuous-time modeling ends at the outputs of the blocks that simulate the baseband mixers and the integrate-and-dump registers. The PLL is modeled in discrete time downstream of the integrate-and-dump registers.

The two dashed-line connections in Fig. 7 allow for the possibility of simulating a semicodeless L2 P(Y) PLL. They feed the output of the L1 carrier NCO along with the L1 signal (prior to data bit mixing) into the block that simulates the L2 baseband mixer and its integrate-and-dump register. These extra inputs are needed in order to simulate how the semicodeless soft decision Z-tracking algorithm generates and uses the estimated $Y(t)$ signal in order to compute L2 accumulations, as per Eqs. (20)-(22).

Simulation of Baseband Mixing and Integrate-and-Dump Operations. The blocks that simulate baseband mixing and the integrate-and-dump registers evaluate integrals that approximate the accumulation computations. Except for the case of L2 semicodeless tracking, the in-phase and quadrature processing that occurs in these blocks can be modeled by the following integrals

$$\breve{I}_k = \frac{1}{\Delta t_k}\int_{t_k}^{t_{k+1}}\{I_{in}(t)\cos[\phi_{PLL}(t)] + Q_{in}(t)\sin[\phi_{PLL}(t)]\}dt \tag{30a}$$

$$\breve{Q}_k = \frac{1}{\Delta t_k}\int_{t_k}^{t_{k+1}}\{I_{in}(t)\sin[\phi_{PLL}(t)] - Q_{in}(t)\cos[\phi_{PLL}(t)]\}dt \tag{30b}$$

where $\breve{I}_k$ and $\breve{Q}_k$ are the perfect noise-free values of the in-phase and quadrature accumulations, which are the outputs of the block. The in-phase and quadrature quantities $I_{in}(t)$ and $Q_{in}(t)$ that appear in the integrands of Eqs. (30a) and (30b) are the inputs to the left-hand side of the baseband-mixing/integrate-and-dump block. For the L1 channel, these quantities take on the values

$$I_{in\mathrm{L1}}(t) = d_{bit}(t)\{I_{sc\mathrm{L1}}(t)\cos[\phi_{\Delta\rho\mathrm{L1}}(t)] - Q_{sc\mathrm{L1}}(t)\sin[\phi_{\Delta\rho\mathrm{L1}}(t)]\} \tag{31a}$$

$$Q_{in\mathrm{L1}}(t) = d_{bit}(t)\{I_{sc\mathrm{L1}}(t)\sin[\phi_{\Delta\rho\mathrm{L1}}(t)] + Q_{sc\mathrm{L1}}(t)\cos[\phi_{\Delta\rho\mathrm{L1}}(t)]\} \tag{31b}$$

where $\phi_{\Delta\rho\mathrm{L1}}(t) = -\Delta\rho(t)\omega_{\mathrm{L1}}/c$ is the L1 carrier phase component that is caused by accumulated delta range. The formulas for the L2 channel are similar, except that they lack the navigation data bit:

$$I_{in\mathrm{L2}}(t) = I_{sc\mathrm{L2}}(t)\cos[\phi_{\Delta\rho\mathrm{L2}}(t)] - Q_{sc\mathrm{L2}}(t)\sin[\phi_{\Delta\rho\mathrm{L2}}(t)] \tag{32a}$$

$$Q_{in\mathrm{L2}}(t) = I_{sc\mathrm{L2}}(t)\sin[\phi_{\Delta\rho\mathrm{L2}}(t)] + Q_{sc\mathrm{L2}}(t)\cos[\phi_{\Delta\rho\mathrm{L2}}(t)] \tag{32b}$$

with $\phi_{\Delta\rho\mathrm{L2}}(t) = -\Delta\rho(t)\omega_{\mathrm{L2}}/c$.

The time integrals in Eqs. (30a) and (30b) are carried out using cubic spline representations of the integrands. Given a cubic spline that is represented by the function's values and first time derivatives at a set of grid points, it is straightforward to perform the exact analytical integration of the function over a defined interval of integration. Furthermore, given a chosen set of grid points for the spline representation, it is straightforward to compute the value and the time derivative of each integrand in Eqs. (30a) and (30b) because the formulas involve trigonometric functions, simple analytically defined phase time histories, and the $I_{sc}(t)$ and $Q_{sc}(t)$ time histories. These latter time histories are themselves defined via a cubic spline, as in Eq. (A.9).

The only remaining question about the evaluation of the integrals in Eqs. (30a) and (30b) is the question of which time grid points to use for the spline. The initial choice of spline grid points is the set of grid points used to define the $I_{sc}(t)$ and $Q_{sc}(t)$ splines, the points t_{scm} for $m = 0, \ldots, M\text{-}1$ as defined in the appendix just before Eqs. (A.8a)-(A.8d). Before using these points, however, a check is made of whether the carrier phase difference $\phi_{PLL}(t) - \phi_{\Delta\rho}(t)$ changes by too large of an amount during a spline interval. This angle would be the phase difference between the PLL NCO and the true received signal if there were no scintillations. If this angle rotates too much during a cubic spline interval, then the trigonometric functions $\cos[\phi_{PLL}(t)-\phi_{\Delta\rho}(t)]$ and $\sin[\phi_{PLL}(t)-\phi_{\Delta\rho}(t)]$, which are implicitly used in the integrands of Eqs. (30a) and (30b), will be inaccurately represented by their cubic splines. Therefore, extra spline points are added between the t_{scm} points, if needed, in order to ensure that $|[\phi_{PLL}(t_{sp(l+1)})-\phi_{\Delta\rho}(t_{sp(l+1)})] - [\phi_{PLL}(t_{spl})-\phi_{\Delta\rho}(t_{spl})]| \le \Delta\phi_{max}$ for all pairs of adjacent spline grid points t_{spl} and $t_{sp(l+1)}$. A reasonable upper limit for this phase change is $\Delta\phi_{max} = 0.4\pi$ rad (1/5 of a cycle).

If the phase error $\phi_{PLL}(t) - \phi_{\Delta\rho}(t)$ changes too much during an accumulation interval, then this is an indication of loss of frequency lock. The power in the $\breve{I}_k$ and $\breve{Q}_k$ accumulations becomes very small in this case. Spline techniques could be used to precisely compute these small

values. The $\Delta\phi_{max}$ limitation on rotation would dictate the use of an inordinate number of spline points in this case. This choice would lead to a greatly increased computation time for a situation in which accurate simulation is not worthwhile. Therefore, the simulation arbitrarily assigns the output accumulation values $\breve{I}_k = 0$ and $\breve{Q}_k = 0$ if the phase error $\phi_{PLL}(t)$ - $\phi_{\Delta\rho}(t)$ rotates by more than 8π rad (4 cycles) during any portion of an accumulation interval.

Integrals different from those in Eqs. (30a) and (30b) are required for simulation of the accumulations that are computed by the semicodeless L2 soft decision Z tracking algorithm. The modified integrals take the form

$$\breve{I}_{\mathrm{L2}k} = \frac{1}{\Delta t_k}\int_{t_k}^{t_{k+1}}\{I_{in\mathrm{L2}}(t)\cos[\phi_{PLL2}(t)] + Q_{in\mathrm{L2}}(t)\sin[\phi_{PLL2}(t)]\}I_{Y1}(t)dt \quad (33a)$$

$$\breve{Q}_{\mathrm{L2}k} = \frac{1}{\Delta t_k}\int_{t_k}^{t_{k+1}}\{I_{in\mathrm{L2}}(t)\sin[\phi_{PLL2}(t)] - Q_{in\mathrm{L2}}(t)\cos[\phi_{PLL2}(t)]\}I_{Y1}(t)dt \quad (33b)$$

Use of the function $I_{Y1}(t)$ in these integrals simulates the effect of estimating the W bits based on L1 quadrature accumulations in order to approximate the P(Y) code, as in Eqs. (20)-(22). The multiplications by $I_{Y1}(t)$ in Eqs. (33a) and (33b) are analogous to the code wipe-off multiplications involving the estimated P(Y) code that occur in an actual semicodeless L2 receiver. The $I_{Y1}(t)$ time history is generated via linear interpolation between values that are defined at the end points of the accumulation intervals. The end-point values are

$$I_{Y1k} = I_{sc\mathrm{L1}}(t_k)\cos[\Delta\hat{\phi}_{\mathrm{L1}k} + \phi_{PLL1k} - \phi_{\Delta\rho\mathrm{L1}}(t_k)] + Q_{sc\mathrm{L1}}(t_k)\sin[\Delta\hat{\phi}_{\mathrm{L1}k} + \phi_{PLL1k} - \phi_{\Delta\rho\mathrm{L1}}(t_k)] \quad (34a)$$

$$I_{Y1(k+1)} = I_{sc\mathrm{L1}}(t_{k+1})\cos[\Delta\hat{\phi}_{\mathrm{L1}(k+1)} + \phi_{PLL1(k+1)} - \phi_{\Delta\rho\mathrm{L1}}(t_{k+1})] + Q_{sc\mathrm{L1}}(t_{k+1})\sin[\Delta\hat{\phi}_{\mathrm{L1}(k+1)} + \phi_{PLL1(k+1)} - \phi_{\Delta\rho\mathrm{L1}}(t_{k+1})] \quad (34b)$$

The linear interpolation of this function takes the standard form

$$I_{Y1}(t) = I_{Y1k} + [I_{Y1(k+1)} - I_{Y1k}]\left(\frac{t - t_k}{\Delta t_k}\right) \quad (35)$$

for the k^{th} accumulation interval. Note that $I_{Y1}(t)$ is the L1 in-phase integrand that would be used in Eq. (30a) if there were no navigation data bits on the L1 channel and if the phase offsets $\Delta\hat{\phi}_{\mathrm{L1}k}$ and $\Delta\hat{\phi}_{\mathrm{L1}(k+1)}$ were both zero. The time integrals in Eqs. (33a) and (33b) are computed using cubic spline approximations of their integrands, as has been discussed in connection with the integration of Eqs. (30a) and (30b).

The use of $\Delta\hat{\phi}_{\mathrm{L1}k}$ and $\Delta\hat{\phi}_{\mathrm{L1}(k+1)}$ in Eqs. (34a) and (34b) constitutes aiding from the L1 PLL Kalman filter, as defined in Section III. This aiding might have been represented in Fig. 7 by an additional dashed line from the L1 PLL to the L2 baseband-mixer/integrate-and-dump block. This simulated aiding serves to make the soft decision Z tracking loop as robust as possible and, therefore, to make the results of this simulation optimistic about the performance of semicodeless tracking. A more conservative version of Eqs. (34a) and (34b) would have used the target stabilized value of $\Delta\phi_{\mathrm{L1}}$ in place of $\Delta\hat{\phi}_{\mathrm{L1}k}$ and $\Delta\hat{\phi}_{\mathrm{L1}(k+1)}$. This value is $\Delta\phi_{des}$, which has been defined in connection with Eqs. (10) and (11).

Simulation of Receiver Thermal Noise. The simulation of receiver thermal noise is straightforward for the L1 C/A and L2C CL tracking loops. The accumulation formulas in Eqs. (30a) and (30b) have been normalized by the integration time, which implies that the average power in the noise-free accumulations $\breve{I}_k$ and $\breve{Q}_k$ is A_0^2. Recall that A_0 is the original amplitude of the complex signal just before it enters the phase screen model of the ionosphere, as in Eq. (25). This average power, the average carrier-to-noise ratio C/N_0, and the accumulation interval Δt_k, can be used to compute the common standard deviation of the in-phase and quadrature noise components ν_{Ik} and ν_{Qk}. For the L1 channel, this common standard deviation is

$$\sigma_{\nu IQ1k} = \frac{A_{0\mathrm{L1}}}{\sqrt{2(C/N_0)_{\mathrm{L1}}\,\Delta t_k}} \quad (36)$$

For the L2C CL channel, the thermal noise power is 3 dB higher relative to the signal power due to the every-other-chip time multiplexing of the CL signal with the CM signal. The noise model for the L2C CL signal reflects this degradation:

$$\sigma_{\nu IQ2k} = \frac{A_{0\mathrm{L2}}}{\sqrt{(C/N_0)_{\mathrm{L2}}\,\Delta t_k}} \quad (37)$$

Given these standard deviations, a Gaussian random number generator can be used to determine the ν_{I1k}, ν_{Q1k}, ν_{I2k}, and ν_{Q2k} noise samples. Note that the very small level of the variations of Δt_k from sample to sample eliminates the need to re-calculate new $\sigma_{\nu IQk}$ values for each new accumulation interval.

The thermal noise model for the semicodeless soft-decision Z tracking of the L2 signal is more complicated. It involves products of the thermal noise on the L1

channel with the signal and the thermal noise on the L2 channel and vice versa. These product terms arise because the $\hat{W}_n$ estimates from Eq. (22) include an L1 signal component and an L1 noise component, and these components of $\hat{W}_n$ get mixed with the L2 signal in order to approximately wipe off the P(Y) PRN code before computation of the L2 accumulations.

These noise products cause the thermal noise in the L2 accumulations to be non-Gaussian. Fortunately, many such products are summed in a typical accumulation interval because the $\hat{W}_n$ estimates and the resulting noise products are computed at an average rate of 480 KHz while the accumulations used in the L2 PLL are computed at a rate of 100 Hz or thereabouts. Therefore, the central limit theorem can be invoked in order to justify using Gaussian models of the net accumulated errors due to the noise product terms.

The Gaussian approximation of the soft-decision Z tracking accumulation noise has a mean of zero and a non-diagonal covariance matrix. The off-diagonal terms result from the presence of L1 noise terms on both the in-phase and quadrature L2 channels, which causes a cross-correlation between ν_{I2k}, and ν_{Q2k}. The noise model's 2x2 covariance matrix is

$$E\left\{\begin{bmatrix}\nu_{I2k}\\ \nu_{Q2k}\end{bmatrix}[\nu_{I2k}\ \nu_{Q2k}]\right\} = \frac{A_{0\mathrm{L1}}^2}{2(C/N_0)_{\mathrm{L1}}\Delta t_k}\begin{bmatrix}\Psi_{11k} & \Psi_{12k}\\ \Psi_{12k} & \Psi_{22k}\end{bmatrix} + \frac{A_{0\mathrm{L2}}^2}{2(C/N_0)_{\mathrm{L2}}\Delta t_k}\left(\Psi_{3k} + \frac{480\times10^3\, A_{0\mathrm{L1}}^2}{2(C/N_0)_{\mathrm{L1}}}\right)\begin{bmatrix}1 & 0\\ 0 & 1\end{bmatrix} \quad (38)$$

where the four new scalar terms in this expression are

$$\Psi_{11k} = \frac{1}{\Delta t_k}\int_{t_k}^{t_{k+1}}\{I_{in\mathrm{L2}}(t)\cos[\phi_{PLL2}(t)] + Q_{in\mathrm{L2}}(t)\sin[\phi_{PLL2}(t)]\}^2\, dt \quad (39a)$$

$$\Psi_{12k} = \frac{1}{\Delta t_k}\int_{t_k}^{t_{k+1}}\{I_{in\mathrm{L2}}(t)\cos[\phi_{PLL2}(t)] + Q_{in\mathrm{L2}}(t)\sin[\phi_{PLL2}(t)]\} \times\{I_{in\mathrm{L2}}(t)\sin[\phi_{PLL2}(t)] - Q_{in\mathrm{L2}}(t)\cos[\phi_{PLL2}(t)]\}dt \quad (39b)$$

$$\Psi_{22k} = \frac{1}{\Delta t_k}\int_{t_k}^{t_{k+1}}\{I_{in\mathrm{L2}}(t)\sin[\phi_{PLL2}(t)] - Q_{in\mathrm{L2}}(t)\cos[\phi_{PLL2}(t)]\}^2\, dt \quad (39c)$$

$$\Psi_{3k} = \frac{1}{\Delta t_k}\int_{t_k}^{t_{k+1}} I_{Y1}^2(t)dt = \frac{I_{Y1k}^2 + I_{Y1k}I_{Y1(k+1)} + I_{Y1(k+1)}^2}{3} \quad (39d)$$

All of the terms in this noise model are products that involve noise power terms or signal terms in the accumulation models of Eqs. (33a) and (33b). These products arise from the signal products that are intrinsic to semicodeless soft decision Z-tracking.

Given the covariance matrix in Eq. (38), ν_{I2k} and ν_{Q2k} samples can be simulated by acquiring two samples from a zero-mean, unit-variance Gaussian random number generator. If these samples are stacked to form a 2x1 column vector, then a left Cholesky factor of the covariance in Eq. (38) can be multiplied by this random column vector in order to synthesize the random vector $[\nu_{I2k},\ \nu_{Q2k}]^{\mathrm{T}}$ in a manner that causes it to have the correct covariance.

The covariance calculation in Eq. (38) and the auxiliary calculations in Eqs. (39a)-(39d) must be re-calculated for each and every simulated accumulation interval because these quantities vary significantly from accumulation to accumulation. The time integrals in Eqs. (39a) to (39c) are computed using cubic spline approximations of their integrands, as already discussed for Eqs. (30a) and (30b). An efficient implementation computes the accumulation integrals in Eqs. (33a) and (33b) and the covariance integrals in Eqs. (39a) to (39c) together in order to exploit the commonality of two of the time histories that are used to form the five integrands.

VI. PLL TRACKING RESULTS FOR ACTUAL AND SIMULATED DUAL-FREQUENCY SCINTILLATIONS

A. Tracking of Experimental Wide-band Scintillation Data

The tracking algorithms described in Section III have been incorporated into the MATLAB software receiver shown in Fig. 5, and they have been applied to the wide-band data that are described in Section IV. Figure 8 shows example tracking outputs for a data set that was collected starting at 00:15 UTC on Jan. 17, 2007. The top plot shows the normalized power as a function of time in dB, and the bottom plot shows the de-trended carrier phase in cycles. Phase de-trending had been accomplished by subtracting out a 3rd-order polynomial fit to each 10 minute data batch. The solid blue curves are for the L1 C/A signal, and the dash-dotted red curves are for the L2C CL signal.

The L1 and L2 PLLs appear to have maintained lock through these moderate scintillations. All tracking metrics, such as Q_k vs. I_k plots, confirmed the successful

tracking of the signal without cycle slips or loss of lock.

These are the strongest L2 scintillations that were seen on the PRN 12 signal during the January 2007 data collection campaign. The S_4 values associated with this data are 0.36 on L1 and 0.51 on L2. These S_4 values have been computed using the wide-band/narrow-band power differencing method that is described in Ref. 25, with the wide-band accumulations computed at 100 Hz and the narrow-band accumulations computed at 10 Hz. These scintillations are not very strong. Therefore, one would expect any reasonably robust PLL to track through them.

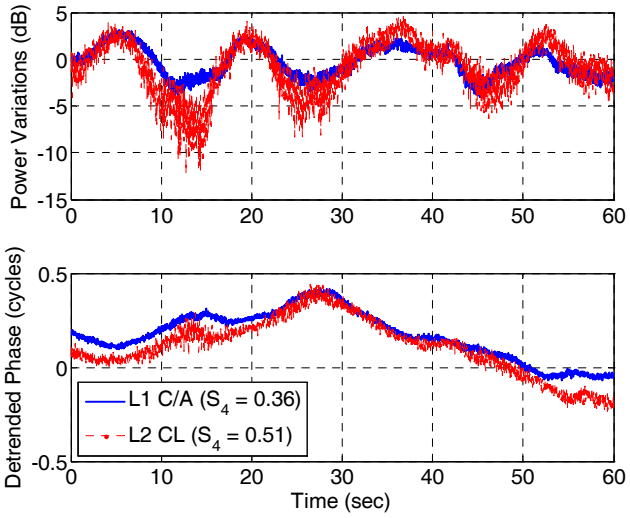

Fig. 8. Experimental dual-frequency scintillation tracking results for PRN 12, normalized power (top plot) and de-trended carrier phase (bottom plot).

The authors were disappointed not to see stronger scintillations that could have more fully exercised this paper's PLL tracking algorithms. They had hoped to see S_4 levels above 0.9, as were observed during an earlier L1 wide-band data collection campaign that was conducted in Cachoeira Paulista, Brazil in December 2003 [10].

Despite the relative mildness of their S_4 levels, these data serve to confirm several important facts. First, they show an obvious strong correlation between the L1 and L2 frequencies of the amplitude fades and the phase variations [*]. This is what the phase screen model in Eq. (27) predicts at moderate S_4 levels. Second, the peak L2 power fades are deeper than those of the L1 signal, which causes the L2 S_4 index to be larger than the L1 value. This verifies another prediction of the phase screen model, one that should be valid at all S_4 levels.

These data will provide useful initial inputs to a rudimentary ionospheric scintillation diffraction tomography algorithm. One can use the "frozen, drifting" ionosphere assumption in order to translate amplitude and phase time histories at a single receiver into spatial amplitude and phase profiles that might have been measured simultaneously by a linear array of receivers, as in Fig. 1. These profiles can be input to a tomography algorithm in order to test whether a single ionospheric density profile can be generated that fits the recorded data at both GPS frequencies.

B. PLL Tracking Performance in Simulated Strong Scintillations

The physics-based phase screen simulation has been used to test the PLLs of Section III in severe scintillation conditions. All three PLLs have been tested, the L1 C/A signal PLL that must deal with unknown navigation data bits, the L2C PLL that uses the CL pilot signal in order to avoid the signal squaring which is inherent in data bit wipe-off, and the semicodeless L2 P(Y) tracking algorithm that is representative of current civilian dual-frequency receivers.

Figure 9 presents results for these three PLLs in the presence of moderately strong L1 scintillations (S_4 = 0.70) and severe L2 scintillations (S_4 = 1.00). The upper plot of this figure shows the scintillating power time histories expressed in dB relative to the average power, and the bottom plot shows the carrier phase error time histories in cycles. Errors can be computed because the "truth" phase is known from the simulation. The "truth" phase includes the effects of accumulated delta range and of scintillations. The simulation duration is 1000 seconds.

The L1 C/A PLL tracks the signal very well, as evidenced by the blue curve in the bottom plot of Fig. 9. It experiences no cycle slips. This is because the L1 scintillations are only moderate. The expected mean time between cycle slips for this PLL has been estimated to be 83 sec based on the analysis of Ref. 11. This implies that the new L1 C/A PLL is somehow much better than the standard PLLs that were considered in Ref. 11.

The L2C CL PLL experiences 2 full cycle slips during this simulation, as shown by the red curve in Fig. 9's lower plot. This PLL has more trouble than does the L1 PLL because the L2 scintillations are much more severe than the L1 scintillations, as evidenced by their higher S_4 value and lower correlation time, τ_0 as defined Ref. 11.

The L2C CL PLL does better than the semicodeless L2 P(Y) PLL. The latter PLL experiences 5 cycle slips, as evidenced by the black curve on the lower plot of Fig. 9. This black curve also appears to have more noise on it than does the red curve. The L2C CL PLL is more robust

[*] The de-trended carrier phase time histories include the effects of receiver clock variations. Some of the phase correlations between the L1 and L2 signals could be caused by the receiver clock rather than the scintillations.

because the CL code is known, which allows this PLL to avoid the squaring loss that is inherent in semicodeless techniques.

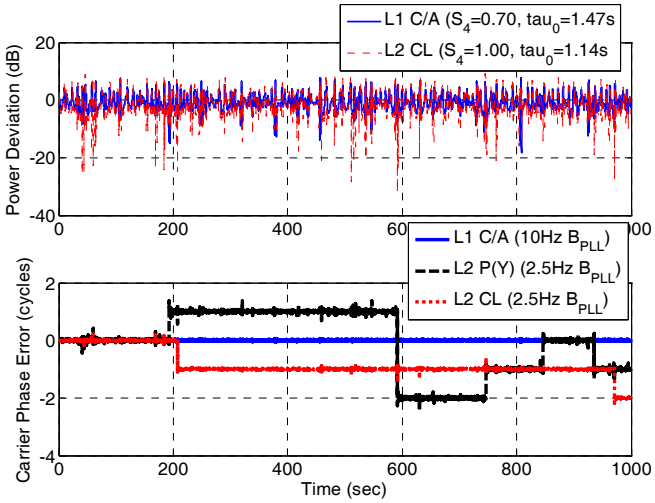

Fig. 9. Simulated PLL tracking results through moderate L1 scintillations and strong L2 scintillations, normalized power (top plot) and carrier phase error (bottom plot)

A surprising result is that the semicodeless L2 P(Y) PLL does not experience complete loss of frequency lock in this case. Experience during actual scintillations suggests that current civilian dual-frequency receivers would not do as well as the performance that is exhibited by the black curve in Fig. 9 [4,5]. There are several possible reasons for this improved simulation performance. The simulated average C/N_0 for the P(Y) signal on L1 and L2 may be slightly higher than is typical. This simulation used the average values C/N_0 = 46 dB-Hz for the L1 P(Y) signal and C/N_0 = 44 dB-Hz for the L2 P(Y) signal. Another possible reason is that the simulation does not include the phase jitter that would be caused by a poor receiver oscillator. Yet a third possibility is that the new Kalman-filter-based PLLs for the L1 C/A signal and for the L2 P(Y) signal are superior to existing PLLs, either by virtue of their architectures or by virtue of their tunings. If this latter explanation is the primary reason for the surprisingly good simulated performance of the semicodeless L2 PLL, then the scintillation tracking robustness of existing civilian dual-frequency receivers may be improvable through modest software changes.

An interesting feature of Fig. 9 is the apparent reason for the first cycle slip of the L2 P(Y) semicodeless PLL. It occurs just after t = 192 sec. There is no L2 power fade evidenced at this time in the dash-dotted red curve of the figure's top plot, but there is a deep power fade in the solid blue L1 curve on the top plot. This correlation implies that the L1 fade caused the slip, which is entirely possible because of the cross-correlation computations that are part of the semicodeless tracking algorithm. By contrast, the two cycle slips of the L2C CL PLL correlate closely with abrupt power fades on the L2 signal (compare the red curves on the figure's two plots).

The bandwidth B_{PLL} = 2.5 Hz has been used for both L2 PLL simulations of Fig. 9, but the higher bandwidth B_{PLL} = 10 Hz has been used for the L1 PLL. The 10 Hz bandwidth was initially preferred because it is the recommended bandwidth from Ref. 11 for scintillation tracking. It has been found, however, that the new PLLs of the present paper are more robust in very strong scintillations at the lower bandwidth 2.5 Hz. In another tracking simulation run that used the same scintillation profile as has been used in Fig. 9, the use of B_{PLL} = 10 Hz caused the L2C CL PLL to completely lose frequency lock.

A second simulation case with increased scintillation severity is presented in Fig. 10. These scintillations have higher S_4 values and lower τ_0 values than those associated with Fig. 9 -- S_4 = 0.97 on L1 and 1.08 on L2. Otherwise, this plot is similar to Fig. 9. This new case reveals several interesting properties of the relative performance of the various PLLs.

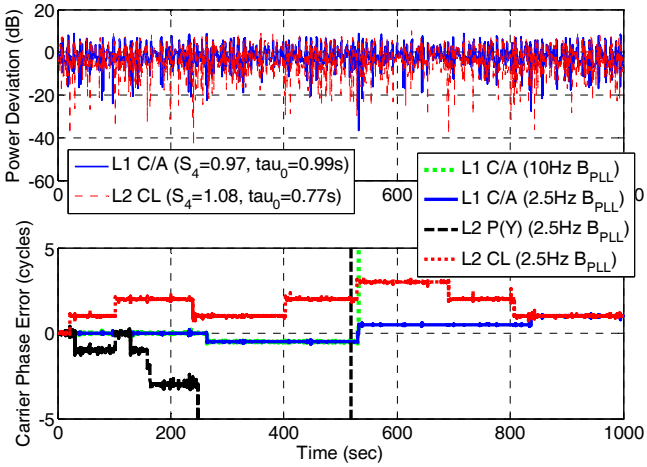

Fig. 10. The simulated effects of extremely severe scintillations on L1 and L2 PLL tracking, normalized power (top plot) and carrier phase error (bottom plot)

The L1 C/A PLL with B_{PLL} = 10 Hz matches the B_{PLL} = 2.5 Hz PLL out to 532 sec, but then it completely loses frequency lock (compare the solid blue curve on the lower plot with the dotted green curve). The blue curve experiences 3 cycle slips that can come in multiples of half-cycles due to the L1 data bits, but it never loses frequency lock. This result at L1 confirms the similar result at L2 that was found for the scintillations associated with Fig. 9: The Kalman filter PLLs of Section III have increased tracking robustness during severe scintillations if their bandwidths are decreased from B_{PLL} = 10 Hz to B_{PLL} = 2.5 Hz.

Another interesting feature of the blue curve is that its number of cycle slips is markedly lower than the mean value of 50 slips that is predicted by Ref. 11 for the S_4 and τ_0 values of this case's L1 signal. This is further evidence that the new PLLs of Section III have better tracking robustness during scintillations than do the standard PLLs that were considered in Ref. 11.

According to Ref. 11, the L1 scintillations in this case are comparable in severity to the L2 scintillations of Fig. 9 because their (S_4, τ_0) combinations yield nearly identical approximate predictions of the mean time between cycle slips. The L1 C/A PLL with B_{PLL} = 2.5 Hz has 3 cycle slips in Fig. 10 versus only 2 slips for the L2C CL PLL in Fig. 9. Although not statistically conclusive, these results suggest somewhat improved tracking robustness for the L2C CL PLL, which is what is expected. On the other hand, one must be careful not to falsely conclude that the L1 C/A squaring loop is better than the L2 CL non-squaring loop based on simple comparisons of cycle slips for the same scintillation event, e.g., based on comparing the solid blue and dotted red curves on the bottom plot of Fig. 10. As shown in the real data and in the simulations, the same event produces more severe scintillations at L2 than at L1, thus, one would expect the L2 tracking to be more challenged for a given common scintillation event.

The L2C CL PLL has performance that is far superior to that of the semicodeless L2 P(Y) soft decision Z-tracking PLL. The semicodeless PLL starts to slip cycles almost immediately, it has an obviously noisier phase error, it wanders more than 5 cycles away from "truth" in less than 250 sec, and it completely loses frequency lock just after t = 515 seconds (consider the black dashed curve on the bottom plot of Fig. 10). Although the L2C CL PLL experiences a number of cycle slips, it never loses frequency lock (see the red dotted curve on the bottom plot of the figure).

VII. SUMMARY AND CONCLUSIONS

This paper has developed PLLs with the aim of increasing their carrier tracking robustness during equatorial scintillations, and it has evaluated these PLLs using both experimental scintillation data and a physics-based simulation. This effort has focused on ways to exploit the new civilian L2C CL signal in hopes of greatly improving the ability of dual-frequency civilian GPS receivers to maintain carrier lock on the L2 signal during strong scintillations. The facts that the CL PRN codes are known and that they are pilot codes both contribute to increased tracking robustness through the elimination of squaring losses that would be incurred if the PLL had to deal with unknown encryption chips, unknown navigation data bits, or both. An additional improvement has been to use a Kalman-filter-based PLL architecture. It discards the idea of a traditional discriminator feedback structure and replaces it with a structure in which the 2π ambiguity of the two-argument arctangent function is unwound by using the filter's *a priori* state estimate.

A second contribution of this work has been the development of a physics-based simulator of dual-frequency scintillations and their impact on PLL tracking performance. This simulator uses a spatial distribution of TEC in the ionosphere that includes fine-scale irregularities of the type that are likely to produce scintillations. It uses a phase screen model in order to compute the effects of these irregularities on the L1 and L2 carrier signals that are received at the ground. It uses an ionospheric drift model in order to translate a spatial scintillation pattern into a temporal pattern. One version of the simulation implements a model of the current best semicodeless L2 P(Y) carrier tracking loop in order to provide a point of comparison for the new L2C CL tracking loop.

Test results on experimental dual-frequency scintillation data show good tracking performance of the new PLLs, but the recorded scintillations exhibit only moderate S_4 values, 0.36 on the L1 frequency and 0.51 on L2. These data validate features of the physics-based simulation model: They show correlations of the power fades and of the dynamic phase variations between the two frequency bands during scintillations with low to moderate levels of S_4. They also show significantly higher S_4 levels on the L2 signal in comparison to the L1 signal for the same scintillation event.

Simulation tests on severe scintillations demonstrate the efficacy of the new L2C CL tracking loop and of the new Kalman-filter-based PLL architecture in general. The new L2 PLL starts to experience intermittent cycle slipping as S_4 gets near 1, and the mean time between slips decreases to something on the order of 100 sec if S_4 = 1.08 and if the scintillation correlation time is τ_0 = 0.77 sec. This performance is far superior to that of a semicodeless civilian tracking loop for the L2 P(Y) signal, which completely loses frequency lock under such conditions. The new Kalman filter PLL architecture also appears to offer increased scintillation tracking robustness for the L1 C/A signal. The tracking robustness of this architecture during severe scintillations is sensitive to the tuning of its loop bandwidth, and a bandwidth of 2.5 Hz is better than a bandwidth of 10 Hz, which is contrary to experience with traditional PLL architectures.

APPENDIX. GENERATION OF $I_{sc}(t)$ AND $Q_{sc}(t)$ SCINTILLATION TIME HISTORIES USING FFT AND SAMPLED-DATA TECHNIQUES

Spatial Frequency Definition that Avoids Aliasing Problems

FFT calculations are used at several points in this appendix, and it is important to properly define the spatial frequencies associated with each spatial FFT. This

definition avoids the possibility that frequency aliasing will give rise to erroneous results. Suppose that the N signal samples $z_0, z_1, z_2, ..., z_{N-1}$ are defined at the N equally spaced grid points $x_n = (-0.5N+n)\Delta x$ for $n = 0, 1, 2, ..., N-1$. The quantity Δx is the grid spacing in meters. Suppose, also, that the number of samples N is a power of 2. The spatial FFT of the signal profile $z_0, z_1, z_2, ..., z_{N-1}$ is the set of complex-valued numbers $Z_0, Z_1, Z_2, ..., Z_{N-1}$. These FFT outputs define component amplitudes and phases at the component spatial frequencies $\Omega_0, \Omega_1, \Omega_2, ..., \Omega_{N-1}$, which are given in rad/m. These frequencies are defined to be

$$\Omega_n = \begin{cases} \dfrac{2\pi n}{N\Delta x} & \text{if } n \le N/2 \\ \dfrac{2\pi(n-N)}{N\Delta x} & \text{if } N/2 < n \end{cases} \qquad \text{(A.1)}$$

throughout this appendix. This explicit definition of the spatial FFT frequencies eliminates the well known aliasing ambiguity in which Ω_n can be replaced by $\Omega_n + l2\pi/\Delta x$ for any integer l without affecting the FFT result.

Two parts of the phase screen calculation would be problematic if aliasing were allowed to occur. One of these parts is a frequency squaring operation that is used in the evaluation of the Huygens-Fresnel integral in Eq. (27). The other part is an IFFT differentiation that is used to determine the derivatives of $\tilde{I}_{sc}(x;\omega)$ and $\tilde{Q}_{sc}(x;\omega)$ in order to develop a cubic spline interpolation between grid points. The frequency definition in Eq. (A.1) restricts the Ω_n values to the lowest frequency range that is compatible with the FFT definition, $|\Omega_n| \le \pi/\Delta x$. This restriction implements the most reasonable physical assumption among all the possibilities that are implied by aliasing.

Generation of a Filtered Random *TEC*(*x*) Profile on a Spatial Grid

The generation of the $I_{sc}(t)$ and $Q_{sc}(t)$ scintillation time histories starts with the generation of the $TEC(x)$ profile at the spatial grid points x_n for $n = 0, 1, 2, ..., N-1$, as defined above. Call these values TEC_n for $n = 0, 1, 2, ..., N-1$. Initially, a Gaussian random number generator is used to generate the values TEC_{Gn} for $n = 0, 1, 2, ..., N-1$ by sampling N uncorrelated values from a distribution with a mean of 0 and a variance of 1. These values are next filtered as in Eq. (28). The spatial filtering process takes the FFT of the TEC_{Gn} values in order to compute $FTEC_{Gn}$ for $n = 0, 1, 2, ..., N-1$. The calculation re-scales these values by the filter response amplitude in order to form the values $FTEC_{Un} = FTEC_{Gn}/[1 + (|\Omega_n|/\Omega_{min})^p]^{0.5}$ for $n = 0, 1, 2, ..., N-1$. It applies the IFFT algorithm to the values $FTEC_{Un}$ in order to compute the un-scaled filtered values TEC_{Un} for $n = 0, 1, 2, ..., N-1$. Lastly, the values TEC_{Un} are re-scaled in order to achieve the target standard deviation σ_{TEC} by using the formula

$$TEC_n = \frac{\sigma_{TEC}}{\frac{1}{N}\sqrt{\sum_{l=0}^{N-1} TEC_{Ul}^2}} TEC_{Un} \quad \text{for } n = 0, 1, 2, ..., N-1 \qquad \text{(A.2)}$$

The FFT operations used to compute $\tilde{I}_{sc}(x;\omega)$ and $\tilde{Q}_{sc}(x;\omega)$ make the implicit assumption that TEC_n is periodic with period N. Precautions are taken in order to avoid any ill effects that otherwise might result from this unnatural periodicity assumption. These precautions are enforced by dividing the x_n grid into 7 regions. These regions are defined in Table A.1 by their respective index sets.

Table A.1. Definitions, Operations, and Uses of 7 Regions of the Spatial FFT Grid.

Index Set of Region	Region Name	Action Taken in Region
$n = 0, ..., N_z-1$	Lower zero-TEC region	Set $TEC_n = 0$ to enforce periodicity
$n = N_z, ..., N_z+N_T-1$	Lower region of TEC tapering to zero	Replace original TEC_n by $TEC_n(n-N_z)/N_T$
$n = N_z+N_T, ..., N_z+2N_T-1$	Lower buffer region	Leave TEC_n unchanged, but discard $\tilde{I}_{sc}(x_n;\omega)$ and $\tilde{Q}_{sc}(x_n;\omega)$ results
$n = N_z+2N_T, ..., N-N_z-2N_T-1$	Usable region	Leave TEC_n unchanged and use $\tilde{I}_{sc}(x_n;\omega)$ and $\tilde{Q}_{sc}(x_n;\omega)$ results
$n = N-N_z-2N_T, ..., N-N_z-N_T-1$	Upper buffer region	Leave TEC_n unchanged, but discard $\tilde{I}_{sc}(x_n;\omega)$ and $\tilde{Q}_{sc}(x_n;\omega)$ results
$n = N-N_z-N_T, ..., N-N_z-1$	Upper region of TEC tapering to zero	Replace original TEC_n by $TEC_n(N-N_z-1-n)/N_T$
$n = N-N_z, ..., N-1$	Upper zero-TEC region	Set $TEC_n = 0$ to enforce periodicity

The idea of the 7 regions in Table A.1 is to place three buffer-type zones before the useable region and an additional three buffer-type regions after the usable region. The first and last of these 6 buffer-type zones

have $TEC = 0$. The second and second-to-last regions have random *TEC* variations whose power gradually increases from 0 at their outer edges to the full power σ_{TEC}^2 at their inner edges. The third and third-to-last buffer-type regions, the ones that are called "Lower buffer region" and "Upper buffer region" in the table, have the full *TEC* power, but the computed $\tilde{I}_{sc}(x;\omega)$ and $\tilde{Q}_{sc}(x;\omega)$ values below these ionospheric regions are not used in the simulation because the non-standard *TEC* profiles from the other two buffer-type regions might spill over to affect the $\tilde{I}_{sc}(x;\omega)$ and $\tilde{Q}_{sc}(x;\omega)$ values in these regions. The central region, the one labeled "Usable region" in the table, has the full *TEC* power and is sufficiently remote from the first two and last two non-full-*TEC*-power regions to produce useable $\tilde{I}_{sc}(x;\omega)$ and $\tilde{Q}_{sc}(x;\omega)$ values for purposes of simulation. In order for the usable region to be sufficiently remote from the first two and last two regions, it is necessary that the width of its neighboring buffer regions, $N_T\Delta x$, be sufficiently large. This condition will be satisfied if this width is much larger than the Fresnel length scale $\sqrt{z\lambda}$, i.e., $N_T\Delta x >> \sqrt{z\lambda}$. For the examples considered here, the buffer zone width $N_T\Delta x = 3000$ m has been used. The ionospheric distance has been set to $z = 350\text{x}10^3$ m. Therefore, the Fresnel length scales are $\sqrt{z\lambda_{L1}} = 260$ m and $\sqrt{z\lambda_{L2}} = 290$ m, and the buffer limit is satisfied.

FFT/IFFT Evaluation of the Huygens-Fresnel Integral

Given TEC_n for $n = 0, ..., N\text{-}1$, the next step in generating $I_{sc}(t)$ and $Q_{sc}(t)$ is to compute $\tilde{I}_{sc}(x_n;\omega)$ and $\tilde{Q}_{sc}(x_n;\omega)$ for $n = 0, ..., N\text{-}1$ along with their derivatives with respect to x. These operations are accomplished by using FFT and IFFT techniques. This calculation starts by computing

$$\phi_{scn} = (2\pi)^2\left[\frac{40.3\,TEC_n}{c\omega}\right] \quad \text{for } n = 0, ..., N\text{-}1 \qquad \text{(A.3)}$$

as in Eq. (24).

The next part of this calculation is to FFT the spatial profile $exp\{j\phi_{sc0}\}$, $exp\{j\phi_{sc1}\}$, $exp\{j\phi_{sc2}\}$, ..., $exp\{j\phi_{sc(N-1)}\}$. Let the FFT output sequence be called Φ_{sc0}, Φ_{sc1}, Φ_{sc2}, ..., $\Phi_{sc(N-1)}$. These values are next multiplied term-by-term by the Fourier transform given in Eq. (29) to yield the transform sequence

$$\Gamma_{scn} = \Phi_{scn}e^{jz\Omega_n^2/(2k)} \quad \text{for } n = 0, ..., N\text{-}1 \qquad \text{(A.4)}$$

In this procedure, one must be careful to use the Ω_n definition given in Eq. (A.1) because the squaring of this frequency will yield anomalous results of aliased alternative values of Ω_n are used in Eq. (A.4).

Finally, the sequence Γ_{sc0}, Γ_{sc1}, Γ_{sc2}, ..., $\Gamma_{sc(N-1)}$ is passed through an IFFT operation to yield the sequence Θ_{sc0}, Θ_{sc1}, Θ_{sc2}, ..., $\Theta_{sc(N-1)}$, and this last sequence is multiplied by a complex re-scaling factor in order to yield the desired outputs

$$\tilde{I}_{sc}(x_n;\omega) + j\tilde{Q}_{sc}(x_n;\omega) = A_0e^{-jkz}\Theta_{scn} \quad \text{for } n = 0, ..., N\text{-}1 \qquad \text{(A.5)}$$

Computation of the derivatives of $\tilde{I}_{sc}(x_n;\omega)$ and $\tilde{Q}_{sc}(x_n;\omega)$ with respect to x relies on the definition of the IFFT operation. Suppose that it is defined as follows

$$\Theta_{scn} = \frac{1}{N}\sum_{m=0}^{N-1}\Gamma_{scm}e^{j\Omega_m n\Delta x} \quad \text{for } n = 0, ..., N\text{-}1 \qquad \text{(A.6)}$$

as in MATLAB. Then the derivative computation is based on a term-by-term differentiation of this series with respect to its $n\Delta x$ argument. The calculation proceeds by taking the IFFT of the sequence $\Gamma'_{scn} = j\Omega_n\Gamma_{scn}$ for $n = 0, ..., N\text{-}1$ in order to compute the sequence Θ'_{sc0}, Θ'_{sc1}, Θ'_{sc2}, ..., $\Theta'_{sc(N-1)}$. This sequence is multiplied by a complex re-scaling factor to yield the derivatives:

$$\left.\frac{d\tilde{I}_{sc}}{dx}\right|_{(x_n;\omega)} + j\left.\frac{d\tilde{Q}_{sc}}{dx}\right|_{(x_n;\omega)} = A_0e^{-jkz}\Theta'_{scn} \quad \text{for } n = 0, ..., N\text{-}1 \qquad \text{(A.7)}$$

Similar to Eq. (A.4), one must use the Ω_n definition given in Eq. (A.1) in order to avoid aliasing problems in this calculation because Ω_n and any aliased version of the form $\Omega_n + l2\pi/\Delta x$ will yield different spatial derivatives.

Translation from Spatial Dependence to Temporal Dependence and Truncation

The spatial profiles defined by $\tilde{I}_{sc}(x_n;\omega)$ and $\tilde{Q}_{sc}(x_n;\omega)$ vs. x_n must be translated into time profiles, and they must be truncated to discard the unusable points. These operations are accomplished by using the ionospheric drift velocity v_{drift} along with the $\tilde{I}_{sc}(x_n;\omega)$ and $\tilde{Q}_{sc}(x_n;\omega)$ samples from the central usable region, as defined in Table A.1.

The temporal scintillation samples are defined on the truncated grid of time points $t_{scm} = (m\text{-}1)\Delta t_{sc}$ for $m = 0, 1, 2, ..., M\text{-}1$. $M = N\text{-}2N_z\text{-}4N_T$ is the total number of grid points in the central usable region of Table A.1, and $\Delta t_{sc} = \Delta x/v_{drift}$ is the uniform spacing of the new temporal grid. The in-phase and quadrature scintillation parameters and their time derivatives at these grid points are

$$I_{scm} = I_{sc}(t_{scm}) = \tilde{I}_{sc}(x_{[m+N_z+2N_T]};\omega) \quad \text{for } m = 0, ..., M\text{-}1 \qquad \text{(A.8a)}$$

$$Q_{scm} = Q_{sc}(t_{scm}) = \widetilde{Q}_{sc}(x_{[m+N_z+2N_T]};\omega) \quad \text{for } m = 0, ..., M\text{-}1 \qquad \text{(A.8b)}$$

$$\dot{I}_{scm} = \dot{I}_{sc}(t_{scm}) = v_{drift} \left.\frac{d\widetilde{I}_{sc}}{dx}\right|_{(x_{[m+N_z+2N_T]};\omega)} \quad \text{for } m = 0, ..., M\text{-}1 \qquad \text{(A.8c)}$$

$$\dot{Q}_{scm} = \dot{Q}_{sc}(t_{scm}) = v_{drift} \left.\frac{d\widetilde{Q}_{sc}}{dx}\right|_{(x_{[m+N_z+2N_T]};\omega)} \quad \text{for } m = 0, ..., M\text{-}1 \qquad \text{(A.8d)}$$

Cubic Spline Interpolation to Yield a Continuous Function of Time

The PLL simulation requires time histories $I_{sc}(t)$ and $Q_{sc}(t)$ that can be evaluated at any point in time. It does not restrict itself to using values only at the grid points associated with Eqs. (A.8a)-(A.8d). Therefore, a cubic spline interpolator has been developed in order to define these time functions. The $I_{sc}(t)$ interpolator takes the following form between the grid points t_{scm} and $t_{sc(m+1)}$:

$$\begin{aligned} I_{sc}(t) &= I_{scm}\left(1 - 3\left[\frac{t-t_{scm}}{\Delta t_{sc}}\right]^2 + 2\left[\frac{t-t_{scm}}{\Delta t_{sc}}\right]^3\right) \\ &+ I_{sc(m+1)}\left(3\left[\frac{t-t_{scm}}{\Delta t_{sc}}\right]^2 - 2\left[\frac{t-t_{scm}}{\Delta t_{sc}}\right]^3\right) \\ &+ \dot{I}_{scm}[t-t_{scm}]\left(1 - 2\left[\frac{t-t_{scm}}{\Delta t_{sc}}\right] + \left[\frac{t-t_{scm}}{\Delta t_{sc}}\right]^2\right) \\ &+ \dot{I}_{sc(m+1)}[t-t_{scm}]\left(-\left[\frac{t-t_{scm}}{\Delta t_{sc}}\right] + \left[\frac{t-t_{scm}}{\Delta t_{sc}}\right]^2\right) \end{aligned} \qquad \text{(A.9)}$$

The cubic spline formula for $Q_{sc}(t)$ takes a similar form.

The PLL simulation needs to compute the first time derivative and the first time integral of several cubic splines that are defined as in Eq. (A.9). This equation is a 3rd-order polynomial in t, which makes the needed derivative and integral formulas straightforward to derive.

Summary of Assumptions of FFT-Based Phase Screen Scintillation Model

A number of assumptions have been made in order to use FFT-based techniques to carry out the computations defined by the phase screen scintillation model in Eqs. (24)-(27). Some of these assumptions have already been stated. They are summarized and discussed here in order to ensure that they are clearly understood.

The first two assumptions are needed in order to use FFT computations. One assumes that the spatial variations in $TEC(x)$ are periodic with period $N\Delta x$. The other assumes that the spatial bandwidth of the $TEC(x)$ variations is limited to the Nyquist band $-\pi/\Delta x \le \Omega \le \pi/\Delta x$ rad/m. These assumptions allow the Fourier transform of $TEC(x)$ to be represented by a finite series of Dirac delta functions of the form $\delta(\Omega - \Omega_n)$ for $n = 0, ..., N\text{-}1$. The coefficients of these delta functions are the outputs of the FFT operation.

A typical grid spacing that has been used is $\Delta x = 0.7$ m. The corresponding spatial frequency upper limit allows power content at frequencies that are 2 orders of magnitude above the frequency associated with the Fresnel length scale. Therefore, the frequency restriction imposed by sampling does not constitute a significant source of modeling error.

A third assumption is that the computed $\widetilde{I}_{sc}(x_n;\omega)$ and $\widetilde{Q}_{sc}(x_n;\omega)$ samples from the central usable region of the FFT grid are not significantly influenced by the periodicity assumption for $TEC(x)$ or by the low levels of $TEC(x)$ variation power that exist in the outer four buffer zones of Table A.1. This assumption will be valid if the inner buffer zones around the central usable regions are wide enough, i.e., if , $N_T\Delta x >> \sqrt{\tilde{z}\lambda}$, and if there is not too much power content in $TEC(x)$ at high spatial frequencies. This latter condition will normally be satisfied due to the filtering of $TEC(x)$ that is defined by Eq. (28).

A fourth assumption is that the temporal variations of the scintillations, as detected by a ground-based receiver, are the result of drift of a "frozen" $TEC(x)$ past the ionospheric pierce point of the LOS vector from the receiver to the GPS spacecraft. This assumption correctly describes a significant percentage of the observed scintillation dynamics of a signal, but it is not entirely valid because the $TEC(x)$ profile deforms over time even when viewed in a coordinate system that drifts with the average ionospheric velocity [7]. This assumption is used because it simplifies the calculations and yields results that retain a reasonable degree of realism.

A fifth assumption is that the cubic spline interpolation defined in Eq. (A.9) accurately reproduces the band-limited signal. This assumption is not strictly valid because a cubic spline is not a perfect band-limiting interpolation filter. The additional "soft" band-limiting inherent in Eq. (28), if coupled with a sufficiently small choice of the FFT grid spacing Δx, will make the cubic spline in Eq. (A.9) approximate any band-limited signal to a degree of accuracy that is more than sufficient for the purposes of the present study.

ACKNOWLEDGEMENT

This work has been supported in part by the NSF through grant No. ATM-0720209. Cassandra G. Fesen is the grant monitor.

REFERENCES

1. Aarons, J., "Global Morphology of Ionospheric Scintillations," *Proc. of the IEEE*, 70(4), 1982, pp. 360-378.
2. Kintner, P.M., Kil, H., and de Paula, E., "Fading time scales associated with GPS signals and potential consequences", *Radio Science*, 36(4), 2001, pp. 731-743.
3. Humphreys, T.E., Psiaki, M.L., Kintner, P.M. Jr., and Ledvina, B.M., "GPS Carrier Tracking Loop Performance in the presence of Ionospheric Scintillations," *Proc. ION GNSS 2005*, Long Beach, CA, Sept. 13-16, 2005, pp. 156-167.
4. Datta-Barua, S., Doherty, P.H., Delay, S.H., Dehel, T., and Klobuchar, J.A., "Ionospheric Scintillation Effects on Single and Dual Frequency GPS Positioning," *Proc. ION GPS/GNSS 2003*, Portland, OR, Sept. 9-12, 2003, pp. 336-346.
5. Dehel, T., Lorge, F., Warburton, J., and Nelthropp, D., "Satellite Navigation vs. the Ionosphere: Where Are We, and Where Are We Going?," *Proc. ION GNSS 2004*, Long Beach, CA, Sept. 21-24, 2004, pp. 375-386.
6. Ledvina, B.M., Makela, J.J., and Kintner, P.M., "First Observations of Intense GPS L1 Amplitude Scintillations at Midlatitude," *Geophysical Research Letters*, 29(14), 2002, pp. 4-1 - 4-4.
7. Kintner, P.M., Ledvina, B.M., de Paula, E.R., and Kantor, I.J., "The Size, Shape, Orientation, Speed, and Duration of GPS Equatorial Anomaly Scintillations," *Radio Science*, 39(2), Art. No. RS2012, 2004.
8. Beach, T.L., and Kintner, P.M., "Simultaneous Global Positioning System Observations of Equatorial Scintillations and Total Electron Content Fluctuations", *Journal of Geophysical Research*, 104(10), 1999, pp. 22553-22565.
9. Ledvina, B.M., Psiaki, M.L., Kintner, P.M., and de Paula, E.R., "Scattering Altitude Estimation Using Closely-Spaced GPS Receivers" *Proc. 11th International Ionospheric Effects Symposium*, Alexandria, VA, May 3-5, 2005.
10. Humphreys, T.E., Ledvina, B.M., Psiaki, M.L., and Kintner, P.M. Jr., "Analysis of Ionospheric Scintillations Using Wideband GPS L1 C/A Signal Data," *Proc. ION GNSS 2004*, Long Beach, CA, Sept. 21-24, 2004, pp. 399-407.
11. Humphreys, T.E., Psiaki, M.L., Ledvina, B.M., Cerruti, A.P., and Kintner, P.M., "Characterization of Severe Ionospheric Scintillation and its Effect on GPS Carrier Phase Tracking," submitted to the *IEEE Trans. on Aerospace and Electronic Systems*, in review.
12. Anon., "Navstar GPS Space Segment/Navigation User Interfaces", IS-GPS-200, Revision D, ARINC Engineering Services, El Segundo, CA, Dec. 2004.
13. Yeh, K.C., and Liu, C.-H., "Radio Wave Scintillations in the Ionosphere," *Proc. of the IEEE*, 70(4), 1982, pp. 324-360.
14. Pidwerbetsky, A.P., "Simulation and Analysis of Wave Propagation through Random Media," Cornell University Ph.D. Thesis in Applied and Engineering Physics, 1988, pp. 17-18.
15. Woo, K.T., "Optimum Semicodeless Carrier-Phase Tracking of L2," *Navigation*, 47(2), 2000, pp. 82-99.
16. Psiaki, M.L., "Smoother-Based GPS Signal Tracking in a Software Receiver," *Proc. ION GPS 2001*, Salt Lake City, Utah, Sept. 11-14, 2001, pp. 2900-2913.
17. Psiaki, M.L., and Jung, H., "Extended Kalman Filter Methods for Tracking Weak GPS Signals," *Proc. ION GPS 2002*, Portland, OR, Sept. 24-27, 2002, pp. 2539-2553.
18. Brown, R.G., and Hwang, P.Y.C., *Introduction to Random Signals and Applied Kalman Filtering, 3rd Edition*, J. Wiley & Sons, (New York, 1997), pp. 190-228.
19. Bar-Shalom, Y., Li, X.-R., and Kirubarajan, T., *Estimation with Applications to Tracking and Navigation*, J. Wiley & Sons, (New York, 2001), pp. 200-232.
20. Jung, H., Psiaki, M.L., and Powell, S.P., "Kalman-Filter-Based Semi-Codeless Tracking of Weak Dual-Frequency GPS Signals," *Proc. ION GPS/GNSS 2003*, Portland, OR, Sept. 9-12, 2003, pp. 2515-2523.
21. Ledvina, B.M., Psiaki, M.L., Powell, S.P., and Kintner, P.M., "Real-Time Software Receiver Tracking of GPS L2 Civilian Signals using a Hardware Simulator," *Proc. ION GNSS 2005*, Long Beach, CA, Sept. 13-16, 2005, pp. 1598-1610.
22. Psiaki, M.L., "Block Acquisition of Weak GPS Signals in a Software Receiver," *Proc. ION GPS 2001*, Salt Lake City, Utah, Sept. 11-14, 2001, pp. 2838-2850.
23. Psiaki, M.L., "FFT-Based Acquisition of GPS L2 Civilian CM and CL Signals," *Proc. ION GNSS 2004*, Long Beach, CA, Sept. 21-24, 2004, pp. 457-473.
24. Klobuchar, J.A., "Ionospheric Effects on GPS," in *Global Positioning System: Theory and Applications, Vol. I*, Parkinson, B.W., and Spilker, J.J. Jr., eds., American Institute of Aeronautics and Astronautics, (Washington, 1996), pp. 485-515.
25. Van Dierendonck, A.J., and Arbesser-Rastburg, B. "Measuring Ionospheric Scintillation in the Equatorial Region Over Africa, Including Measurements From SBAS Geostationary Satellite Signals," *Proc. ION GNSS 2004*, Long Beach, CA, Sept. 21-24, 2004, pp. 316-324.